Effect of aspect ratio on flow through and around a porous disk

Tingting Tang,[1,2,3,4] Jin Xie,[4,5] Shimin Yu,[1,4,6] Jianhui Li,[4] and Peng Yu[1,2,3,4,*]

[1]*Shenzhen Key Laboratory of Complex Aerospace Flows, Southern University of Science and Technology, Shenzhen 518055, China*

[2]*Guangdong Provincial Key Laboratory of Turbulence Research and Applications, Southern University of Science and Technology, Shenzhen 518055, China*

[3]*Center for Complex Flows and Soft Matter Research, Southern University of Science and Technology, Shenzhen 518055, China*

[4]*Department of Mechanics and Aerospace Engineering, Southern University of Science and Technology, Shenzhen 518055, China*

[5]*University of Science and Technology of China, Hefei 230022, China*

[6]*Harbin Institute of Technology, Harbin 150001, China*

(Received 29 January 2021; accepted 10 June 2021; published 6 July 2021)

We numerically investigated steady axisymmetric flow through and around a porous disk with aspect ratio (χ) ranging from 1 to 20, Reynolds number (Re) varying from 10 to 120, and Darcy number (Da) ranging from 10^{-6} to 1. The wake characteristics are presented in terms of the streamline patterns, the geometrical parameters as well as the occurrence of the recirculating wake. In particular, the bifurcation curves in the Re-Da parametric space can be collapsed onto approximately the same curve for all χ when the modified χDa is used. Both χ and Da are demonstrated to be closely related to the drag and have similar effects on the flow behavior. The formation mechanism of recirculating wake at different χ is further discussed with respect to the base bleed quantified by the flow rate as well as the vorticity accumulation and decay.

DOI: 10.1103/PhysRevFluids.6.074101

I. INTRODUCTION

Permeable bluff bodies immersed in fluid flow are widely seen in nature and engineering applications, such as the insect wings (Thrips) composed of filaments [1], the dandelion clock made of numerous florets [2], the "flocs" of material in liquid-solid reactors [3], and the permeable scaffold for transporting nutrients in bioreactors [4]. The above-mentioned porous media are usually simplified as nonaxisymmetric or axisymmetric porous bodies in experimental or numerical studies.

There are several studies on flow through and around a nonaxisymmetric porous cylinder. Noymer *et al.* [5] studied the effects of Reynolds number (Re) and Darcy number (Da) on the drag exerted on a permeable circular cylinder by using both numerical and experimental methods. For the two-dimensional (2D) numerical study, Re was set to 10, 100, 1000, and Da ranged from 10^{-6} to 10; for the experimental tests, Re varied from 800 to 10 000 and Da was set to 1.7×10^{-5}, 6.6×10^{-5}. The computational results were in good agreement with experimental results. Between low and high extremes in permeability, a distinct dependence of the drag on Re was observed. More recently, Bhattacharyya *et al.* [6] numerically (2D) studied the drag and wake of a porous circular cylinder in low-Re flow by using a more generalized Brinkman-Darcy-Forchheimer equation. Yu *et al.* [7] reported 2D numerical results on the steady wake structure behind a porous circular cylinder and

*yup6@sustech.edu.cn

provided more abundant information on the intermediate wake behaviors, i.e., the recirculating wake is either detached from or penetrated into the permeable body. Yu *et al.* [8] and Valipour *et al.* [9] also studied 2D flow through and around porous square and diamond-square cylinders, respectively, in the parameter space of Re and Da. Though different shaped bodies were considered [7–9], the wake behaviors were found to be quite similar, for instance, under a certain range of the Da, the wake initially increases but then decreases in size with increasing Re, and eventually disappears when Re is sufficiently large. The relevant 2D pore-scale study [10] also supports the findings with modified permeability. Ledda *et al.* [11] studied 2D flow past and around a rectangular cylinder via linear stability analysis. The neutral stability curves also presented similar trends for the base flow and the qualitative behaviors remained the same for all the investigated thickness-to-height ratios.

For axisymmetric geometries, the body shape can be characterized by the aspect ratio (χ) defined as the ratio of the maximum diameter and the thickness measured along the axis of revolution. Typical axisymmetric bodies include sphere, spheroid, and disk. Neale *et al.* [12] analytically studied the creeping flow through permeable spheres via the 2D Darcy equation and found that the drag of a permeable body was smaller than its impermeable counterpart. Masliyah and Polikar [3] conducted experiments for a porous sphere with porosity of 0.98 for both low and high Re, the results of which were later demonstrated to be compared well with the three-dimensional (3D) numerical solution of the Brinkman-extended Darcy equation [13]. Yu *et al.* [14] studied the wake structure of steady flow past and around a porous sphere by using 2D simulations and found that the recirculating wake may penetrate deeper with increasing Re for $\mathrm{Da} \leqslant 10^{-4}$, which might be applied to the nutrient transport from the surrounding culture medium into a scaffold. The previous studies of flow through and around a porous spheroid are mainly focused on the 3D analytical solution in the Stokes flow regime, e.g., Refs. [15–17].

Comparatively, there has been much less research on flow through and around a porous disk although the permeable disklike geometry is widely seen in nature (e.g., the dandelion pappus [2], the permeable insect wing [1], the disklike canopy as well as the firebrand) and in physical applications (e.g., the small flying vehicle [18], the porous scaffold [4], the wind farm [19], and the parachute). Liu *et al.* [20] conducted experiments for flow past a honeycomb disk with $\chi = 5$ at $\mathrm{Re} = 10^4$. Two recirculation regions were observed: the smaller region right behind the rear of the disk, which is separated by small jets through the disk into several species; and the larger region located further downstream, which is comparably smaller than the recirculation zone behind a solid disk. Cummins *et al.* [21] numerically (2D) investigated the flow through and around a permeable disk for Re ranging from 10 to 130, Da varying from 10^{-9} to 1, and fixed $\chi = 10$. Three flow regimes were observed: in regime I ($\mathrm{Da} \leqslant 10^{-6}$), the wake is characterized by the presence of a toroidal vortex whose length is approximately equal to that of an impervious disk; in regime II ($10^{-6} < \mathrm{Da} \leqslant 10^{-3}$), the vortex decreases in size and moves further downstream with increasing Da; in regime III ($\mathrm{Da} > 10^{-3}$), no recirculation region is formed. The description is also qualitatively consistent with that of the other porous bodies. More recently, Ledda *et al.* [22] studied the flow dynamics of an anisotropic and nonhomogeneous rigid porous thin disk, which resembled the morphology of a dandelion pappus, by using the linear stability analysis technique (3D). The results demonstrated that the flow could be characterized by a separated, steady, and axisymmetric recirculating vortex ring if the mean porosity was beyond a certain threshold.

The impermeable axisymmetric bodies of sphere and flat disk were also studied previously by using 3D numerical simulations [23,24] and experimental tests [25], where the differences in flow transition, instability, and drag between sphere and flat disk were analyzed. Meliga *et al.* [26] numerically (3D) studied the wake of a flat disk ($\chi = 10^3$) and found that all nonlinear interactions between modes took place in the recirculation bubble. Gao *et al.* [27] numerically (3D) studied the flow around an inclined solid disk with fixed $\chi = 50$ and focused on the bifurcation sequences in the parametric space of Re and the inclination angle. From 3D computations, Shenoy and Kleinstreuer [28] also indicated that the transition process in the range of $10 \leqslant \mathrm{Re} \leqslant 300$ for a solid disk ($\chi = 10$) differs from that for a sphere as they observed a loss of symmetry plane in the third regime due to a twisting motion of the axial vorticity strands in the wake of a disk. Auguste

et al. [29] numerically (3D) investigated the dynamics in the wake of a relatively thick circular disk ($\chi = 3$). Five nonaxisymmetric regimes were defined in the range of $150 \leqslant \mathrm{Re} \leqslant 280$, including the states similar to those identified in the flow around a sphere or an infinitely thin disk, and a new state characterized by the existence of two distinct frequencies.

Besides, the effects of χ on the impervious axisymmetric bodies were demonstrated to be significant. Chrust *et al.* [30] numerically (3D) studied the transition in the wake of both oblate spheroids and flat cylinders or disks and found significant similarity between both configurations. Fernandes *et al.* [31] experimentally investigated flat cylinders with $1.5 \leqslant \chi \leqslant 20$ and found that the transition Reynolds number (Re_{cr}) for steady axisymmetric flow is a function of χ, i.e., $\mathrm{Re}_{cr} = 116.5(1 + \chi^{-1})$. For flat disks ($\chi = \infty$), a reasonable consensus has been reached for the value of Re_{cr} between 115 and 117 [23,24,30]. For a disk with $\chi = 10$, Re_{cr} was found to be 135 in Ref. [28] and 129.6 in Ref. [30]. For a thicker disk ($\chi = 3$), Re_{cr} was reported to be approximately 159.4 [27]. Willmarth *et al.* [32] experimentally studied impervious circular disks with multiple χ falling in a viscous fluid at low Re. The motions and wakes of freely falling disks exhibit systematic dependence on Re and the dimensionless moment of inertia, which are largely affected by the aspect ratio of the disk.

Since χ largely influences the behavior of flow around an impervious disk, it is reasonable to predict that χ also has nonnegligible effects on the wake structure behind a porous disk. Also, the porous disk can be regarded as a solid counterpart when the macroscopic permeability is extremely small. As far as we know, the effects of χ on the flow past and around a porous disk are not fully understood yet, which should be significant since it alters the drag exerted by the flow in the porous medium. Nevertheless, the flow behaviors with various χ are expected to be similar in terms of the occurrence of the recirculating wake, as implied for the above-mentioned nonaxisymmetric and axisymmetric porous bodies. Accordingly, the present study aims to, on the one hand, identify the distinct flow features for various χ, and, on the other hand, understand the common wake behaviors for all χ as well as the underlying wake formation mechanism. The present study is expected to provide complementary information about the effects of aspect ratio with respect to the previous study [21] on flow through and around a permeable disk (with fixed $\chi = 10$). Also, the present work intends to constitute an analogy to the previous study [11] on flow through and around 2D rectangular cylinders with various aspect ratios.

The rest of the paper is organized as follows. In Sec. II, the numerical method is described with regards to the geometry configuration, governing equations, computational domain and meshes employed, followed by the verification and validation of the computational setup. In Sec. III, the numerical results and discussion are presented in terms of the streamline pattern, the properties of recirculating wake and drag, the bifurcation diagrams for the wake existence, the flow rate, as well as the vorticity field. Finally, the summary and conclusions are provided in Sec. IV.

II. NUMERICAL METHOD

A. Flow configuration and governing equations

Figure 1(a) shows a 2D axisymmetric flow configuration in the present study. The porous disk is immersed in a uniform flow with velocity U_∞ at zero angle of attack. The coordinates of the reference system are represented by (r, z), where the r axis lies along the radius of the disk and the z axis points in the direction of the freestream velocity. The origin of the system is located in the center of the front surface of a disk. The half section of the porous disk has a radial length of $D/2$ and a vertical thickness of T. The original 3D structure can be recovered by revolving around the axisymmetric line ($r = 0$).

In the present study, the investigated range of $\chi = D/T$ is from 1 to 20. The disk becomes thinner as χ increases, as illustrated in Fig. 1(b). Based on the formula of Re_{cr} (for the transition from steady axisymmetric flow to the regular bifurcation) provided in Ref. [31] for an impermeable disk, the upper limit of $\mathrm{Re} = U_\infty D/\nu$ (ν is kinematic viscosity) is set to be 120 for all χ; and the

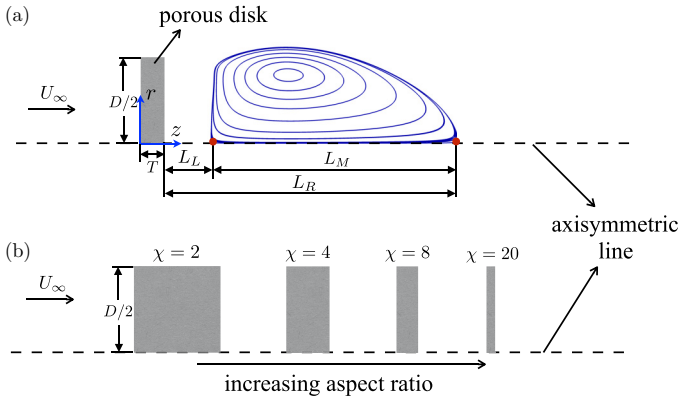

FIG. 1. Sketch of the flow configuration: (a) recirculating wake formed behind a porous disk; (b) examples of the disk with different χ.

investigated lower limit of Re is 10. Although the investigated Re are in the stable regime for solid disks, it is shown in Ref. [22] that porosity/permeability enhances the stability of the wake of thin disks in terms of critical Reynolds number, so it is very probable that the configurations considered here are stable.

For steady axisymmeric flow around a fixed solid disk, it is known that a toroidal vortex may appear behind the disk and attach to the rear surface of the disk for a certain range of Re [28,31]. However, it is found in Ref. [21] as well as in this study that the recirculating wake can be detached from or penetrate into a porous disk, similar to that of flow through and around a nonaxisymmetric body, e.g., Refs. [7,9,11]. The geometrical parameters of L_L and L_R are the downstream distances from the rear surface of the disk to the leading and trailing saddle points of the recirculating wake, respectively. The wake length can thus be calculated as $L_M = L_R - L_L$. The positive and negative values of L_L indicate that the recirculating wake is detached from or penetrate into the porous disk, respectively.

In the clear fluid region, the governing equations for incompressible, steady, Newtonian fluid flow in cylindrical coordinates can be expressed as

$$\frac{1}{r}\frac{\partial(ru_r)}{\partial r} + \frac{\partial u_z}{\partial z} = 0, \tag{1a}$$

$$\frac{1}{r}\frac{\partial(ru_ru_z)}{\partial r} + \frac{\partial(u_zu_z)}{\partial z} = -\frac{1}{\rho}\frac{\partial p}{\partial z} + \frac{\mu}{\rho}\left[\frac{1}{r}\frac{\partial}{\partial r}\left(r\frac{\partial u_z}{\partial r}\right) + \frac{\partial^2 u_z}{\partial z^2}\right], \tag{1b}$$

$$\frac{1}{r}\frac{\partial(ru_ru_r)}{\partial r} + \frac{\partial(u_zu_r)}{\partial z} = -\frac{1}{\rho}\frac{\partial p}{\partial r} + \frac{\mu}{\rho}\left[\frac{\partial}{\partial r}\left(\frac{1}{r}\frac{\partial(ru_r)}{\partial r}\right) + \frac{\partial^2 u_r}{\partial z^2}\right], \tag{1c}$$

where u_r and u_z are the radial and axial velocities in the r and z directions, respectively; p is pressure; ρ represents density; and μ is dynamic viscosity.

In the porous region, where the porous medium is considered to be rigid, homogeneous, isotropic and saturated with the same single-phase fluid as that in the clear fluid region, the governing equations can be expressed as

$$\frac{1}{r}\frac{\partial(r\overline{u_r})}{\partial r} + \frac{\partial\overline{u_z}}{\partial z} = 0, \tag{2a}$$

$$\frac{1}{r}\frac{\partial}{\partial r}\left(\frac{r\overline{u_r}\,\overline{u_r}}{\phi}\right) + \frac{\partial}{\partial z}\left(\frac{\overline{u_z}\,\overline{u_r}}{\phi}\right) = -\frac{1}{\rho}\frac{\partial(\phi p^*)}{\partial r} + \frac{\mu}{\rho}\left[\frac{\partial}{\partial r}\left(\frac{1}{r}\frac{\partial(r\overline{u_r})}{\partial r}\right) + \frac{\partial^2\overline{u_r}}{\partial z^2}\right] - \frac{\mu\phi}{\rho K}\overline{u_r}, \tag{2b}$$

$$\frac{1}{r}\frac{\partial}{\partial r}\left(\frac{r\overline{u_r}\,\overline{u_z}}{\phi}\right)+\frac{\partial}{\partial z}\left(\frac{\overline{u_z}\,\overline{u_z}}{\phi}\right)=-\frac{1}{\rho}\frac{\partial(\phi p^*)}{\partial z}+\frac{\mu}{\rho}\left[\frac{1}{r}\frac{\partial}{\partial r}\left(r\frac{\partial\overline{u_z}}{\partial r}\right)+\frac{\partial^2\overline{u_z}}{\partial z^2}\right]-\frac{\mu\phi}{\rho K}\overline{u_z}. \tag{2c}$$

The present formulation used to model flow in a porous medium can be deducted from the volume averaging theory [33–36] and the control volume principle [37]. Two types of averaging operators were used in the averaging procedure: the superficial average and the intrinsic average. The superficial average of a given variable Ψ in the representative averaging volume V is defined as $\overline{\Psi}=(\int_{V_{fd}}\Psi dV)/V$ and the intrinsic average is defined as $\Psi^*=(\int_{V_{fd}}\Psi dV)/V_{fd}$, where V_{fd} is the volume of fluid. In Eqs. (2a)–(2c), $\overline{u_r}$ and $\overline{u_z}$ are the superficial velocity component in the radial and axial directions, respectively; p^* is the intrinsic pressure, ϕ the porosity, and K the permeability. For simplicity, the averaging notations of $^-$ and * are omitted for variables in porous media in the following sections. The dimensionless form of Eqs. (2a)–(2c) indicates that both Re and $\mathrm{Da}=K/D^2$ are the control parameters of the flow. In the present study, Da is varied from 10^{-6} to 10^{0} to cover a fairly wide range of flow phenomena.

The boundary conditions imposed at the interface between the fluid and the porous medium are expressed as

$$u_r|_f=\overline{u_r}|_p, \tag{3a}$$

$$u_z|_f=\overline{u_z}|_p, \tag{3b}$$

$$\frac{\mu}{\varphi}\frac{\partial\overline{u_t}}{\partial n}\bigg|_p-\mu\frac{\partial u_t}{\partial n}\bigg|_f=\beta_1\frac{\mu}{\sqrt{K}}u_t\bigg|_i+\beta_2\rho u_t^2\bigg|_i, \tag{3c}$$

$$\frac{\mu}{\varphi}\frac{\partial\overline{u_n}}{\partial n}\bigg|_p-\mu\frac{\partial u_n}{\partial n}\bigg|_f=0. \tag{3d}$$

Here, Eqs. (3a) and (3b) describe the continuity of velocity components at the interface; the subscripts of $_f$ and $_p$ represent the fluid and the porous medium, respectively. Equation (3c) is the shear stress jump condition [38], and Eq. (3d) describes the continuity of the normal stress at the interface. The coordinate of n is normal to the interface and the coordinate of t is perpendicular to n. The stress jump parameters of β_1 and β_2 are associated with the excess viscous and inertial stresses, respectively. In the present study, the stress jump parameters are set to zero, and the porosity is fixed at 0.95, which was previously demonstrated to be suitable for low-Re flow through and around a porous bluff body [8,14].

The drag coefficient (C_D) of an impermeable disk can be calculated from [39]

$$C_D=\frac{\boldsymbol{F}\cdot\hat{\boldsymbol{z}}}{1/2\rho U_\infty^2 A_d}, \tag{4}$$

where $\hat{\boldsymbol{z}}$ is the unit vector in the axial direction and A_d is the characteristic frontal area of the disk. The force is expressed as [40]

$$\boldsymbol{F}=\int_{S_d}(p\boldsymbol{I}-\boldsymbol{\tau})\cdot\hat{\boldsymbol{n}}dS_d, \tag{5}$$

where $\boldsymbol{\tau}$ is the stress tensor, $\boldsymbol{I}$ the identity matrix, S_d the surface area of disk, and $\hat{\boldsymbol{n}}$ the unit surface normal vector of the surface. The pressure and viscous drag coefficients (C_{Dp} and C_{Dv}) are calculated in the same way as Eq. (4) using pressure and viscous forces, respectively.

However, the drag calculation based on the surface integration (SI) [Eq. (5)] may not be very accurate for permeable disks since it neglects the change of momentum in fluid through the porous body. Alternatively, the force exerted on the body can be calculated based on the linear momentum balance on a control volume (CV) far away from the surface of the disk. The net force is written as

$$\boldsymbol{F}=\int_{S_c}(p\boldsymbol{I}-\rho\boldsymbol{v}\boldsymbol{v})\cdot\hat{\boldsymbol{n}}dS_c, \tag{6}$$

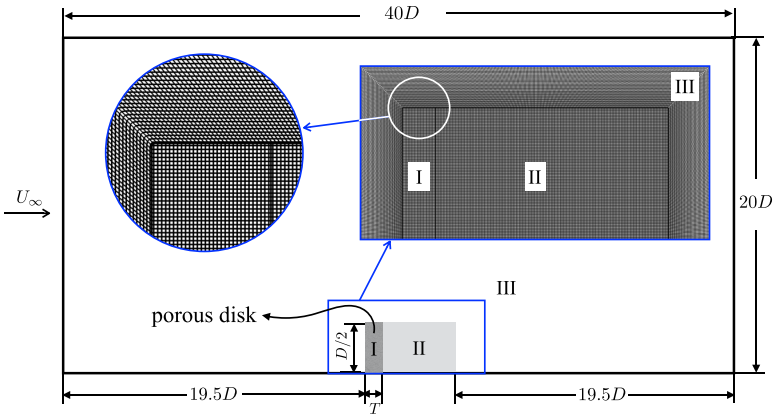

FIG. 2. Sketch of the computational domain and the typical mesh near the interface of the porous and fluid regions.

where S_c is the surface area of the CV and $\boldsymbol{v} = (u_r, u_z)$ the velocity vector. In the present study, both the CV [Eq. (6)] and the SI [Eq. (5)] methods are adopted for drag analyses.

B. Computational domain and grid

The computational domain has a width of $40D$ in the z direction and a height of $20D$ in the r direction, as indicated in Fig. 2. For cases with $\chi > 1$, the whole domain is divided into three blocks: block I is the porous disk region; block II is the fluid region with a width of $D(1 - 1/\chi)$ and the same height as that of block I; block III is the large fluid region outside of blocks I and II. The χ is adjusted by increasing T of block I into block II, with the largest $T = D$ since the smallest investigated χ is one. Blocks I and II are placed in the middle of the lower boundary with a distance of $19.5D$ from the front surface of the disk to the inlet boundary of the whole domain. The distance between the rear surface of the disk and the outlet boundary is sufficiently long compared with the previous studies [21,28]. In the current study, the CV for the drag calculation is $(r, z) \in [0, 20D] \times [10D, 30D]$.

Figure 2 also shows a typical mesh for the present simulations. The uniform orthogonal grids are used in blocks I and II, where the total number of grids is fixed for various χ. The O-type grid is used in block III, where the grid size increases in an exponential fashion from the outer boundaries of blocks I and II to the boundaries of the computational domain. The boundary conditions of the computational domain are as follows: the uniform velocity U_∞ is prescribed at the inlet boundary; the Neumann condition for the velocity is employed at the outlet boundary; the stress-free and axisymmetric conditions are used at the upper and lower boundaries, respectively.

C. Verification and validation

In the present study, the finite volume method was used to solve the governing equations on colocated grids. The pressure-velocity coupling was treated with the SIMPLEC algorithm [41]. The checkerboard instability was avoided by the interpolation method proposed by Rhie and Chow [42]. The detailed numerical treatment for the porous-fluid coupling interface was provided in Ref. [43], thus it is not repeated here.

The grid independence test is first performed for flow around an impermeable disk with $\chi = 10$ by using three sets of grids: 240×270 (coarse), 360×280 (intermediate), and 480×280 (fine). The total number of grids are varied according to the resolution of the first-layer-grid adjacent to the solid wall of the disk. The numerical results of both drag coefficient (C_D) and L_M are produced for $10 \leqslant \mathrm{Re} \leqslant 130$. The percent errors between the coarse and fine grid solution range from 0.3% to

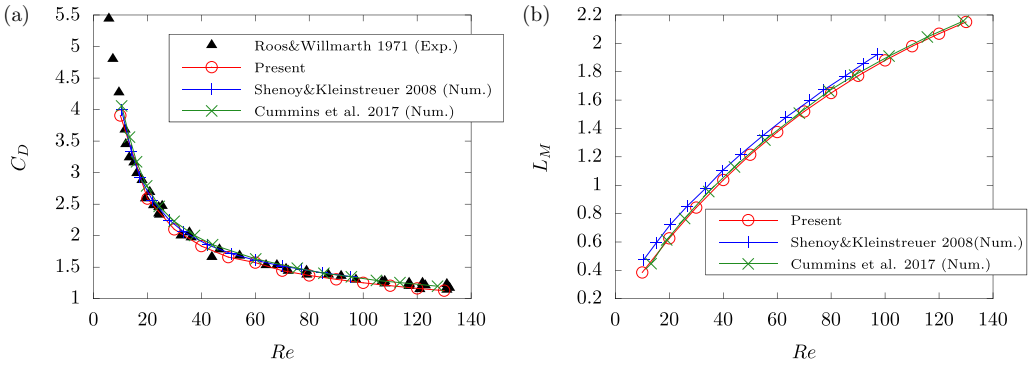

FIG. 3. Comparisons of the present results with the previously reported data (e.g., Roos and Willmarth [25], Shenoy and Kleinstreuer [28], Cummins *et al.* [21]) for flow around an impermeable disk with $\chi = 10$: variations of (a) C_D and (b) L_M with Re.

0.8% for C_D, and from 0.22% to 0.33% for L_M. The percent errors between the intermediate and fine grids are even less, as expected.

The results of the fine grids are presented in Fig. 3. The results are validated through the experimental results in Ref. [25]. The C_D of the present study agrees very well with the experimental result for the investigated range of Re. Following the analysis of Cummins *et al.* [21], the percent errors in the estimate of C_D for $\mathrm{Re} = 10$ and $\mathrm{Re} = 130$ are 0.61% and 3.75%, respectively, compared with the experimental results obtained from the best-fit curve [21]. The error is less than the corresponding validation uncertainty calculated from the numerical and experimental uncertainties. Therefore, the current results are validated at a level of 4.17% for $\mathrm{Re} = 10$ and 4.37% for $\mathrm{Re} = 130$. The 2D results from [21] and 3D results from [28] are also presented for comparison. It is observed that the present results are slightly smaller than those of the previous numerical results, one possible reason of which is that the blockage ratio applied in the present study is smaller, which results in smaller C_D. The blockage effects on C_D were also studied in Refs. [21,44], which indicate the same variation trend as that of the present study. Also, as seen in Fig. 3(b), the current results of L_M agree well with those of the previous studies [21,28], especially well with those of the 2D study [21].

The grid sensitivity test is also performed for flow through and around a permeable disk at fixed $\mathrm{Da} = 2.5 \times 10^{-4}$ and $\chi = 10$. Three sets of meshes are employed for the whole computational domain: 120×600 (coarse), 180×650 (intermediate), and 240×680 (fine). The numerical results demonstrate that the percent errors between the coarse and fine grid are no greater than 0.8% and 0.4% for C_D and L_M, respectively, for the investigated range of Re. The percent errors between successive grids are even smaller. Therefore, the fine grid is guaranteed to produce nearly grid-independent solutions.

The current fine-resolution results for $\chi = 10$, $\mathrm{Re} = 130$ and different Da are also compared with the previous numerical results [21] calculated from the finite element method. Figures 4(a) and 4(b) show that the present results of p and u_z agree very well with the previous results [21] for each Da. The current results at $\mathrm{Da} = 10^{-6}$ compare well with the literature results at $\mathrm{Da} = 10^{-9}$ since both cases are similar to an impermeable situation. The p and u_z upstream of the disk for the present study are slightly smaller than those in Ref. [21], especially at smaller Da, which may be due to the different upstream distance used. Figures 4(c) and 4(d) show the u_z profile with r at fixed $z = D/\chi$ and $z = D(1/\chi + 1)$, respectively. For $r \lesssim D/2$, the u_z compares very well with the literature result; while for $r \gtrsim D/2$, the u_z is noticeably smaller than that in Ref. [21], which is more evident with decreasing Da. This is because the blockage effects on the porous disk with larger Da are smaller due to stronger advection, which is also demonstrated in Ref. [21] when comparing the porous disk and the impermeable disk. The smaller u_z also indicates that the shear stress on top of the disk as well as the C_D of the present study are slightly smaller than those in Ref. [21].

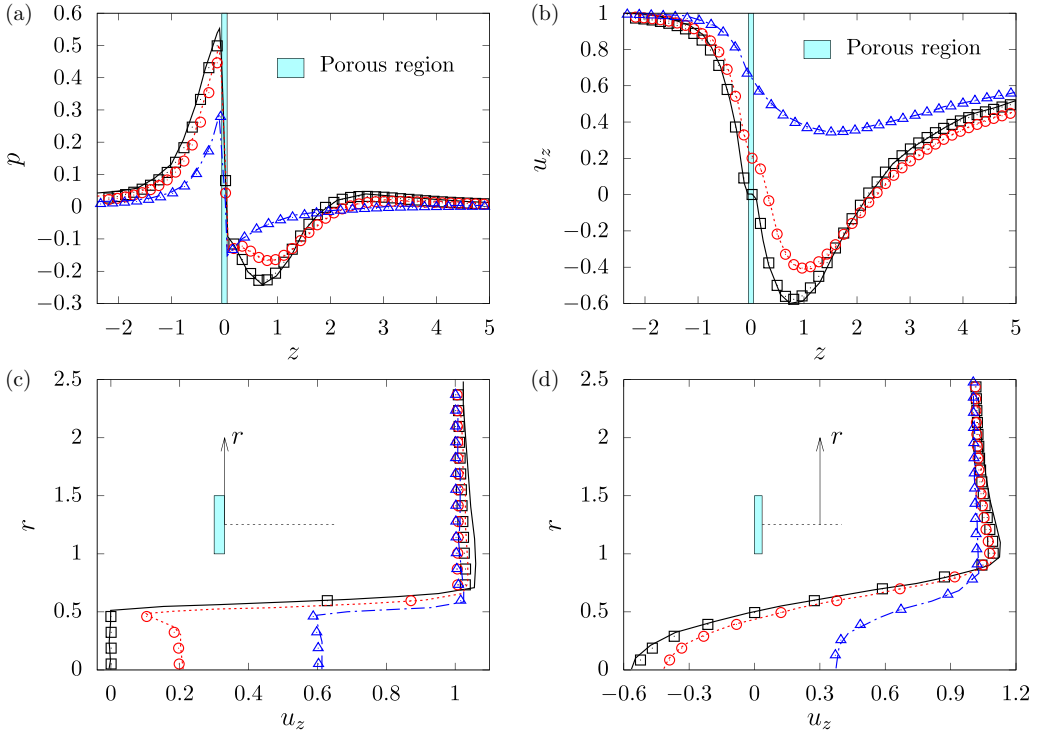

FIG. 4. Verification for flow through and around a permeable disk: (a) p and (b) u_z along the streamwise distance z; (c) u_z along the radial distance r at the rear surface of the disk; (d) u_z along r at the downstream position of $z = D(1/\chi + 1)$. Present results are represented as □ for Da $= 10^{-6}$, ◯ for Da $= 2.5 \times 10^{-4}$, and △ for Da $= 1 \times 10^{-3}$. Results from Cummins *et al.* [45] are represented as solid lines for Da $= 10^{-9}$, dotted lines for Da $= 2.5 \times 10^{-4}$, and dash-dotted lines for Da $= 1 \times 10^{-3}$.

III. RESULTS AND DISCUSSION

A. Flow pattern

The flow pattern can be significantly altered by χ of the porous disk under different Re and Da. Figure 5 shows the streamline and pressure contours at relatively small Da $= 10^{-4}$ for two representative χ and Re. The flow patterns are typical for those at an even smaller Da. For $\chi = 1$, the recirculating wake behind the porous disk, which increases in size with increasing Re, is similar to that of flow around an impermeable disk. Differently, the recirculating wake is observed to penetrate into the porous disk, as seen in Fig. 5(a). This is because the fluid flowing through the disk is largely decelerated by the porous structure of the disk. Within the porous disk, the pressure first decreases in the axial direction of the flow, but then increases in the same direction. The decelerated flow is easily affected by the adverse pressure gradient (APG), which results in flow separation from the axisymmetric line.

The recirculating wake is also closely linked to the flow around the edges of the disk. When the flow is impacting on the front surface of the porous disk, the velocity in the middle of the front surface is greatly decreased and the pressure is highly increased, similar to flow situations at the "stagnation point" on an impermeable wall. As the fluid flows around the edges of the half-disk from the "stagnation point," the pressure first decreases to a very small value near the corner, but then gradually increases along the rest of the edges. A low pressure region also appears at the rear corner, which is mainly due to the relatively weak reverse flow in the "inner" (porous medium) part of the corner compared with the inertial flow in the "outer" (clear fluid) part of the corner. The

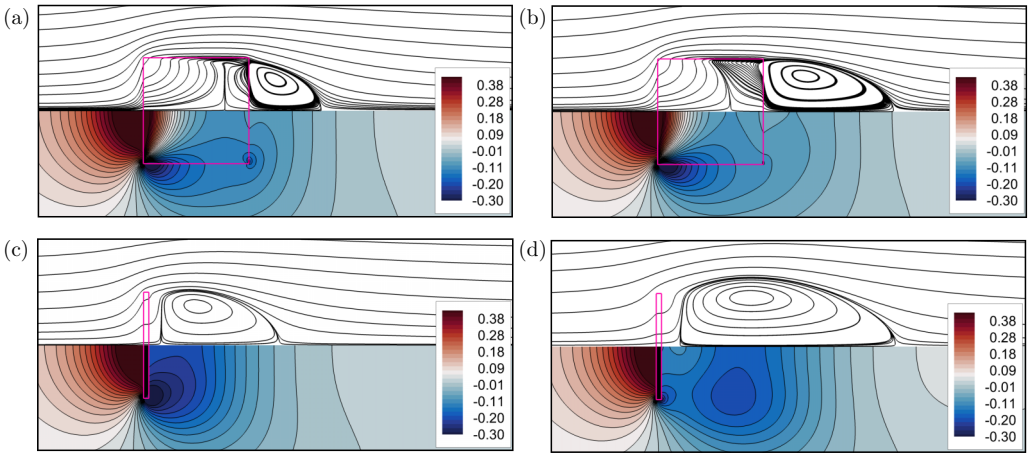

FIG. 5. Streamlines and pressure contours at Da $= 10^{-4}$ for (a) Re $= 50$, $\chi = 1$; (b) Re $= 120$, $\chi = 1$; (c) Re $= 50$, $\chi = 20$; (d) Re $= 120$, $\chi = 20$.

combination of the "outer" and "inner" APG gives rise to the formation of recirculating wake. For Re $= 120$ [Fig. 5(b)], the penetration depth, defined as the distance between the flow separation point within the porous disk and the rear of the disk, is larger and the reverse flow is stronger. Therefore, the secondary decreased pressure region is not formed at the rear corner. The larger penetration depth also indicates that the "inner" APG is mainly caused by the outer inertial flow.

In addition, the penetrating phenomenon was also reported for the porous sphere and the circular cylinder in the previous studies [7,14], but not observed for the porous square cylinder [8]. The penetration is greatly affected by the frictional "side-wall" of the porous body since the viscous boundary layer developed from the porous side wall would retard the flow and provide a chance for the penetrating APG. The side-wall is the wall area that is parallel to the streamwise flow. Another important factor affecting the formation of the penetrating vortex is the amount of inertial fluid flow through the porous body, confronting the APG. Accordingly, a dimensionless parameter r_p indicating the ratio of the inertial to the frictional forces can be defined as $r_p = V_f/V_s$, where V_f and V_s are the differential volume of the inertial fluid and the "side-wall", respectively. Here, $V_s = A_s dt$, where A_s is the differential "side-wall-area" and dt the differential length in the streamwise direction.

Table I summarizes the V_f, V_s, and r_p for various geometries. For 2D nonaxisymmetric bodies, only a slice of fluid with the cross-section area and the differential height in the axial direction dh is considered since the body is assumed to be infinitely long in the axial direction. For circular cylinder, $V_f = ldtdh$, where l is the chord length of the circular cross-section, and $V_s = \pi Ddhdt$, thus $r_p = l/\pi D$. Straightforwardly, we have $V_f = Ddtdh$ and $V_s = 2Ddhdt$ for square cylinder. As seen in Table I, r_p for circular cylinder is smaller than that of square cylinder as $0 \leqslant l \leqslant D$, implying less resistance to the "side-wall" friction. In other words, the curvature shape of circular cylinder makes it easier for penetration of vortex compared with square cylinder. For 2D axisymmetric bodies, the

TABLE I. The differential volumes of V_f and V_s as well as the ratio r_p for different geometries.

Geometry	Circular cylinder	Square cylinder	Circular disk	Sphere
V_f	$ldtdh$	$Ddtdh$	$0.25\pi D^2 dt$	$0.25\pi l^2 dt$
V_s	$\pi Ddhdt$	$2Ddhdt$	$(\pi D^2/\chi)dt$	$\pi D^2 dt$
r_p	$l/\pi D$	$1/2$	$\chi/4$	$l^2/(4D^2)$

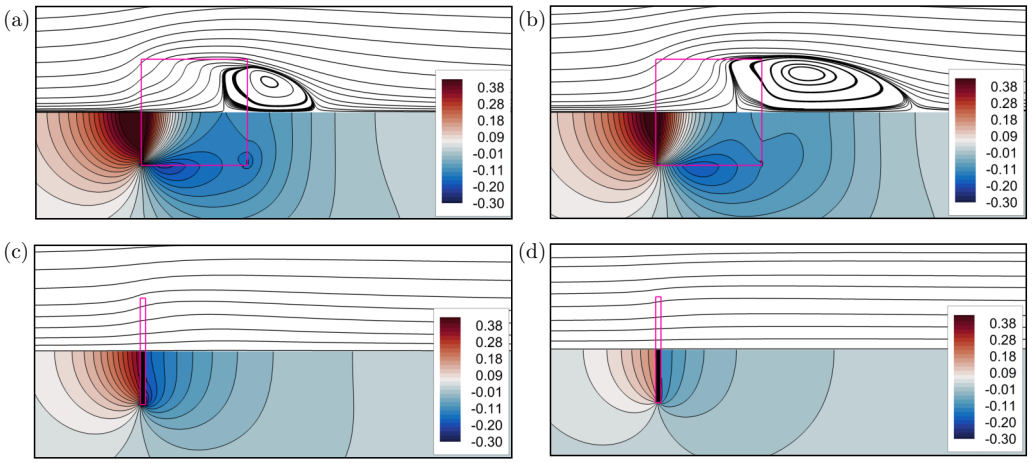

FIG. 6. Streamlines and pressure contours at Da $= 10^{-3}$ for (a) Re $= 50$, $\chi = 1$; (b) Re $= 120$, $\chi = 1$; (c) Re $= 50$, $\chi = 20$; (d) Re $= 120$, $\chi = 20$.

slice of fluid flowing through the body is obstructed by the surrounding "side-wall." Therefore, we have $V_f = 0.25\pi D^2 dt$, $V_s = (\pi D^2/\chi)dt$ for circular disk and $V_f = 0.25\pi l^2 dt$, $V_s = \pi D^2 dt$ for sphere. For $\chi = 1$, the r_p of sphere is no greater than that of circular disk and both geometries show very similar penetration depths $\geqslant 30\%D$. In general, the r_p of sphere and circular disk ($\chi = 1$) are smaller than those of the circular and square cylinders, indicating easier vortex penetration. For larger χ, the situation can be different.

For $\chi = 20$, the recirculating wake no longer penetrates into the porous disk [see Fig. 5(c)] since the r_p is 5, which is much larger than those of the geometries mentioned above. Without much friction drag from the wall, the fluid flows through the disk easily and presents the so-called "based bleed." Accordingly, the recirculating wake is detached from the rear of the disk, as also presented in the previous studies, e.g., Refs. [14,21]. It is also observed that L_M is larger compared with that of $\chi = 1$. Different from Fig. 5(a), the small pressure region at the rear corner becomes larger owing to the more blunt shape of the disk. The pressure within the porous disk also decreases continually without the "inner" APG. For larger Re [Fig. 5(d)], the recirculating wake is much longer and the small pressure region is divided into two parts, one is still at the rear corner, another one moves further downstream in the vortex zone. Here, the recirculating wake is also longer and wider than that shown in Fig. 5(b), the formation mechanism of which is mainly associated with the vorticity accumulation and decay, as will be discussed in Sec. III E.

Figure 6 shows the flow pattern at relatively large Da $= 10^{-3}$. For $\chi = 1$ [Figs. 6(a) and 6(b)], the recirculating wake also penetrates into the porous disk, but with smoother streamlines at the rear surface, compared to the smaller Da cases. The penetration depths along the axial direction for both Re are similar to those at Da $= 10^{-4}$ [Fig. 5(a)] though the total penetration area is comparably smaller. The L_M is also similar to that at a smaller Da for Re $= 50$, but is noticeably larger for Re $=$ 120. This implies that the larger permeability of Da $= 10^{-3}$ may provide even more obstruction to the incoming flow for $\chi = 1$ due to the increasing interaction between the inertial and viscous forces within the porous structure, while for smaller Da most fluid flows around the disk. In Figs. 6(a) and 6(b), the negative pressure peak also moves further downstream due to the stronger advection at larger Da.

For the disk with $\chi = 20$ [Figs. 6(c) and 6(d)], the recirculating wake completely disappears for both Re in contrast to those shown in Figs. 5(c) and 5(d). This suggests that Da $= 10^{-3}$ represents relatively high permeability for $\chi = 20$ with negligible drag, while the same Da means fairly low permeability for $\chi = 1$ with large obstructing effects on the flow. The pressure difference between

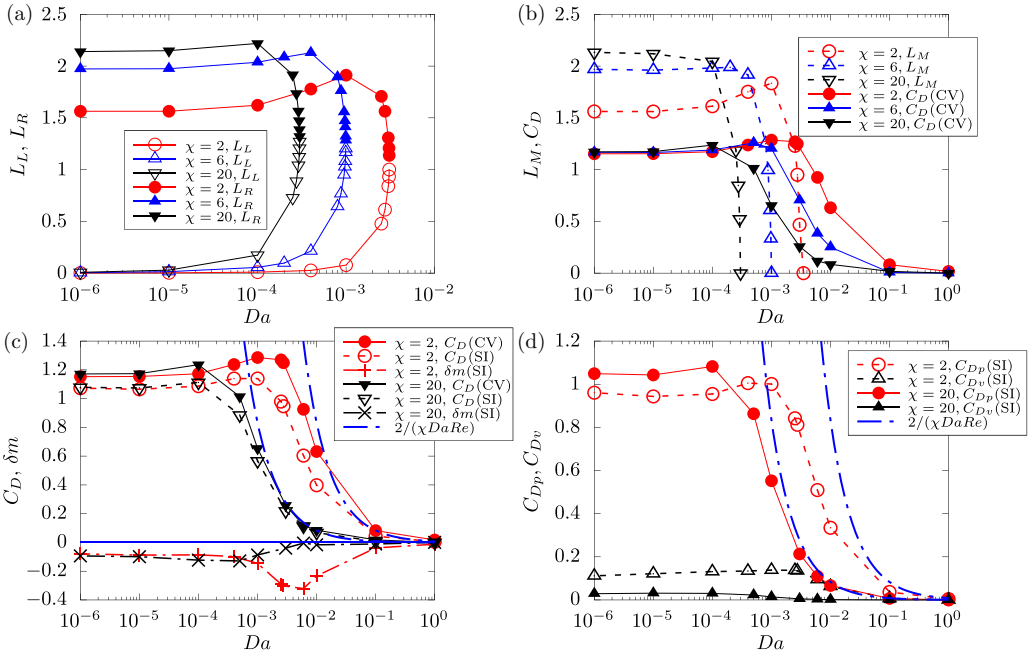

FIG. 7. Variations of (a) L_L, L_R and (b) L_M, C_D (calculated from the CV method) with Da at fixed Re = 120 and different χ as indicated. (c) Comparison of C_D calculated from the CV and SI methods. (d) C_{Dp} and C_{Dv} obtained from the SI method.

the front and rear surface of the porous disk also decreases evidently, compared with the smaller χ case. As Re increases, the streamlines are almost parallel to each other and the pressure contours are almost symmetric around the radial centerline of the porous disk. The increasing inertial forces have opposite influences on the thinner and thicker disks for Da $= 10^{-3}$, which are not observed for Da $= 10^{-4}$.

B. The recirculating wake and drag properties

The dimensionless geometrical parameters of L_L and L_R varying with Da at three representative χ and fixed Re = 120 are shown in Fig. 7(a). One common trend for all χ is that L_L increases with increasing Da, which is mainly due to the larger amount of fluid exiting the rear of the porous disk. Another shared characteristic for all χ is that L_R first increases slowly, until reaching a maximum value, and then decreases rapidly with increasing Da. At maximum Darcy number ($\mathrm{Da_{max}}$), L_R and L_L coincide, indicating the disappearance of recirculating wake. This trend was also observed in the previous studies [21,46] on flow through and around a porous bluff body at relatively large Re. Apart from this, the effects of χ on the L_L-Da and L_R-Da relationships are clearly seen. The evidently increased L_L is observed at larger Da for smaller χ, which is reasonable since it is more difficult for the fluid to penetrate through a thicker porous medium. The L_R at fairly small Da $= 10^{-6}$ is noticeably larger when the disk becomes thinner. Among the presented cases, the L_R of $\chi = 20$ remains the highest for Da $\leqslant 10^{-4}$, but then rapidly decreases with increasing Da. The increasing trend of L_R is more obvious for smaller χ. Also, the $\mathrm{Da_{max}}$ increases as χ decreases. These behaviors are largely related to the drag, base bleed as well as vorticity, as will be discussed later.

The L_M and C_D under the same flow condition are also presented in Fig. 7(b). The variation trend of L_M is somewhat consistent with that of C_D. When C_D gradually increases towards ~1.2, L_M decreases marginally and even increases for larger χ. As C_D begins to decrease noticeably, L_M

decreases sharply at approximately the same Da. The difference of variation trends between the drag and the wake is also evident. For relatively large Da, the wake completely disappears while the drag is still comparable with that at very small permeability. Also, for relatively small permeability, the increasing trend of drag is observed for all χ, but the increasing trend of L_M is only evidently seen at $\chi = 2$. The radial width of the recirculating wake is also found to exhibit similar behaviors with L_M, which is several times smaller than L_M though not shown here.

Figure 7(c) shows C_D calculated from the CV and the SI methods. For both χ, the SI method underestimates C_D in the investigated range of Da since the momentum change (δm) for flow through the porous disk is neglected. At $\chi = 2$, the absolute value of momentum change ($|\delta m|$) first keeps relatively low ($\approxeq 0.08$) for $10^{-6} \leqslant \mathrm{Da} \leqslant 10^{-4}$ then apparently increases to a maximum value at $\mathrm{Da} \approx 5 \times 10^{-3}$ and finally decreases to zero at very large Da. Besides, comparing Figs. 7(b) and 7(c), it is found that $|\delta m|$ reaches the maximum value when the vortex disappears. This is because the viscous base bleed from the rear of the disk and the inertial flow around the disk form an extended shear layer that prevents the APG as well as the reverse flow, which induces additional viscous drag in the form of momentum change. Similar variation trend of δm with Da is also observed for large $\chi = 20$. However, the maximum $|\delta m|$ is much smaller than that of $\chi = 2$ since the effective length scale for the viscous flow around the solid phase is constricted by the small thickness of the disk.

Figure 7(d) presents the components of pressure and viscous drag obtained from the SI method. For both χ, it is seen that C_{Dp} is dominant over C_{Dv} for the whole range of Da. This seems contradictory to the microscopic results reported previously [47] for flow through and around a porous square cylinder, where the viscous drag is even larger than that of the pressure drag for a relatively small solid fraction. The reason is that the C_{Dp} and C_{Dv} integrated from the porous surfaces here are different from those integrated from the surfaces of the solid phase in the porous medium from a microscopic perspective considering that the viscous forces within the porous disk have contributed to the pressure drag macroscopically, i.e., the Darcy force. Another observation is that for all the presented χ, both C_{Dp} and C_{Dv} first increase and then decrease with increasing Da. This is consistent with the trend of the total drag. As indicated above, the increasing trend is mainly due to the strong viscous force within the porous medium. In addition, comparing Figs. 7(b) and 7(d), it is clearly seen that the pressure drag is still large when the wake disappears since C_{Dp} is influenced by both the fluid within and the fluid outside of the porous disk. Therefore, the total drag can be expressed as

$$C_D = \frac{\int_0^T \int_0^{0.5D} (\mu U_a / K) 2\pi r dr dz}{0.5 \rho U_\infty^2 \pi (0.5D)^2} + C'_{Dp} + C_{Dv} + |\delta m|, \tag{7}$$

where U_a is the superficial velocity in the porous disk; C'_{Dp} is the pressure drag due to the vortex behind the porous disk; T is the thickness of the disk. The first term on the right-hand side (RHS) of Eq. (7) describes flow through the porous disk; the other three terms on the RHS account for flow around the disk.

For very high permeability, we have $C'_{Dp}, C_{Dv}, |\delta m| \to 0$ and $U_a \to U_\infty$, so the expression of C_D can be simplified as

$$C_D = \frac{\int_0^T \int_0^{0.5D} (\mu U_\infty / K) 2\pi r dr dz}{0.5 \rho U_\infty^2 \pi (0.5D)^2} = \frac{2}{\chi \mathrm{DaRe}}. \tag{8}$$

Equation (8) can also be derived from the asymptotic analysis referring to the leading order uniform flow [21]. Similar formulas with modified coefficients were reported in Ref. [5] for porous circular cylinder and in Ref. [48] for spheres. The C_D calculated from Eq. (8) is also presented in Fig. 7(d). It is seen that the analytical formula presents better agreement with the numerical results of $\chi = 20$ than those of $\chi = 2$ since the C_{Dv} is almost zero for a larger range of high permeability for $\chi = 20$. Besides, an even better data consistency is observed between the analytical formula and the C_D calculated from the CV method, as shown in Fig. 7(c). This implies that the addition of viscous

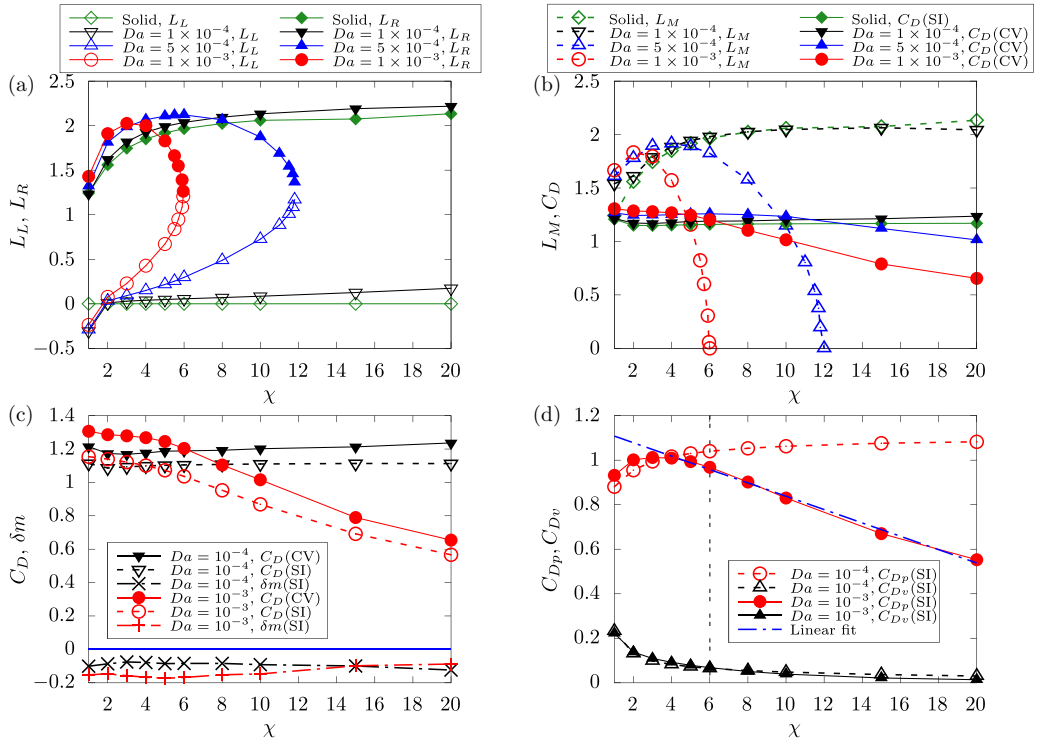

FIG. 8. Variations of (a) L_L, L_R and (b) L_M, C_D (calculated from the CV method) with χ at fixed Re = 120 and different Da as indicated. (c) Comparison of C_D calculated from the CV and SI methods. (d) C_{Dp} and C_{Dv} obtained from the SI method.

forces and $|\delta m|$ may make up for the difference between a finite and an infinite porous medium when the permeability is not extremely high.

Figure 8(a) shows the geometrical parameters L_L, L_R varying with χ for the solid disk as well as the porous disk at different Da. For the solid disk, L_R first increases sharply to $\sim$2 for $1 \leqslant \chi \leqslant 5$, and then increases slightly with increasing χ; L_L is trivially zero since the disk is impermeable. For $\mathrm{Da} = 1 \times 10^{-4}$, the tendency is very similar to that of the solid counterpart except at $\chi = 1$ where the flow penetrates into the porous disk so L_L is negative. Similar trends are also observed for $\mathrm{Da} < 1 \times 10^{-4}$. For $\chi \geqslant 2$, L_L increases slowly and almost linearly with increasing χ. For $\chi > 4$, L_R is ~ 2 and L_L is ~ 0.1, which may remain the same for an infinite thin disk. For larger $\mathrm{Da} = 5 \times 10^{-4}$ and $\mathrm{Da} = 1 \times 10^{-3}$, L_R and L_L form a half closed curve with a maximum $\chi_{\max}$ and the geometrical parameters disappear when $\chi > \chi_{\max}$. The existence range of χ decreases with increasing Da. The trends shown in Fig. 8(a) are somewhat similar to those shown in Fig. 7(a). The corresponding L_M and C_D are also shown in Fig. 8(b). For smaller Da and the solid case, L_M increases monotonically. For relatively large Da, L_M first increases and then decreases rapidly with increasing χ. The L_M decreases to zero at $\chi \approxeq 6$ and $\chi \approxeq 12$ for $\mathrm{Da} = 1 \times 10^{-3}$ and $\mathrm{Da} = 5 \times 10^{-4}$, respectively. The variation trend of the radial width of the recirculating wake is also similar to that of L_M. The decreasing rate of C_D is however much smaller than those shown in Fig. 7(b), consistent with the decreasing rate of L_M.

Figure 8(c) shows C_D calculated from the SI method is smaller than that obtained from the CV method for the whole range of χ at fixed Da, but the variation trends of C_D with χ are consistent for both methods. For higher $\mathrm{Da} = 10^{-3}$, the $|\delta m|$ first increases and then decreases with χ. The largest $|\delta m|$ occurs at $\chi \approxeq 6$, where the vortex disappears. Differently, for lower $\mathrm{Da} = 10^{-4}$, the $|\delta m|$ first

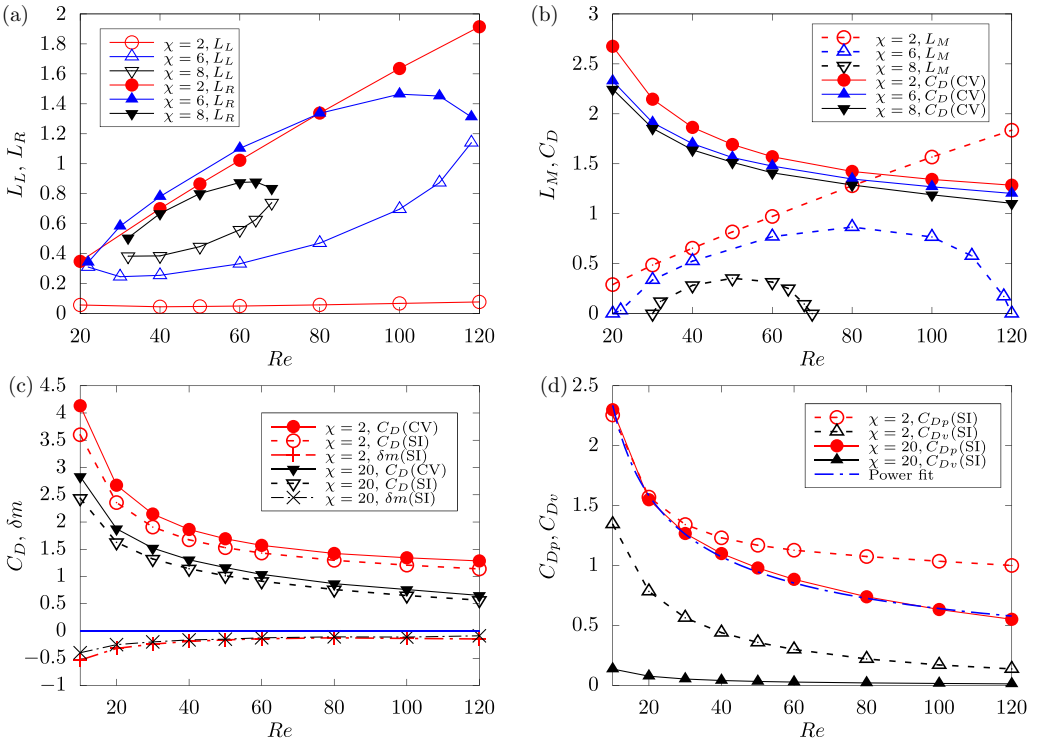

FIG. 9. Variations of (a) L_L, L_R and (b) L_M, C_D (calculated from the CV method) with Re at fixed Da $= 10^{-3}$ and different χ as indicated. (c) Comparison of C_D calculated from the CV and SI methods. (d) C_{Dp} and C_{Dv} obtained from the SI method.

decreases and then increases though not very obvious. The $|\delta m|$ is overall larger for higher Da, as expected. Figure 8(d) shows the variations of C_{Dp} and C_{Dv} with χ. For Da $= 10^{-4}$, C_{Dp} increases with χ due to the larger recirculation zone behind the disk; while C_{Dv} decreases with χ owing to the smaller side surface area. Since the C_{Dp} is dominant over C_{Dv}, the total C_D barely decreases. For Da $= 10^{-3}$, C_{Dp} first increases and then decreases with increasing χ. Apparently, the first increasing C_{Dp} is due to the increasing wake size. It is also observed that C_{Dp} decreases almost linearly with χ for $\chi \geqslant 6$; a linear relationship $C_{Dp} = -0.03\chi + 1.138$ is found, as shown in Fig. 8(d). Differently, C_{Dv} is almost the same for both Da; the decreasing C_{Dv} contributes to the decrease of the total drag at relatively small χ. For $\chi \geqslant 6$, the expression of C_D can be simplified as

$$C_D = \frac{\int_0^T \int_0^{0.5D} (\mu U_a / K) 2\pi r dr dz}{0.5\rho U_\infty^2 \pi (0.5D)^2} = \frac{2U_a}{\chi \mathrm{DaRe} U_\infty}, \tag{9}$$

since the vortex disappears and the contributions from the C_{Dv} and δm are very small. In this case, $C_D \approxeq C_{Dp}$ is mainly described by the Darcy force within the porous medium.

The effects of Re and χ on the geometrical parameters at fixed Da $= 10^{-3}$ are demonstrated in Fig. 9. For $\chi = 2$, L_R increases almost linearly with increasing Re, while L_L is approximately zero for the range of Re. For larger $\chi = 6$, the L_R first increases and then decreases with increasing Re, while the opposite trend is observed for L_L. The existence range of the geometrical parameters decreases as χ further increases to 8. Also, the variation trends of L_R and L_L with Re for various χ (at fixed Da) are very similar to the trends for various Da (at fixed χ), i.e., for relatively small Da, the L_R increases linearly with Re, while for relatively large Da, the L_R first increases and then decreases with increasing Re, as shown in the previous study [2]. Therefore, the χ and Da are considered

TABLE II. Estimations of Da_{max} and Re_{max} for each χ.

χ	1	2	3	5	6	8	10	15	20
Da_{max}	0.00838	0.0044	0.0029025	0.00173	0.001443	0.0010925	0.000883	0.0006	0.000457
Re_{max}	52±1	49±1	48±1	46±1	46±1	45±1	44±1	43±1	42±1

to have similar effects on the geometrical parameters varying with Re. Figure 9(b) shows that L_M increases linearly with Re for $\chi = 2$, while it first increases and then decreases for larger χ. Also, C_D decreases monotonically with Re; C_D is larger for thicker disk, though in general it does not differ much among all χ.

Figure 9(c) also shows the SI method underestimates C_D for the whole range of Re at both small and large χ. The $|\delta m|$ increases with Re for $10 \leqslant \mathrm{Re} \leqslant 50$ and remains nearly constant for $\mathrm{Re} \gtrsim 60$. This is because at small Re, the viscous force is large, which affects a large distance away from the porous disk; at large Re, the opposite occurs. The drag calculated with the SI method is further decomposed into the pressure and viscous drag, as presented in Fig. 9(d). For $\chi = 2$, as Re increases, both C_{Dp} and C_{Dv} decrease due to smaller viscous forces. The larger C_{Dp} at lower Re can also be observed in the flow pattern [Fig. 5(a)], where a small pressure region appears at the rear corner. As Re increases, C_{Dp} becomes more dominant due to the increasing recirculation zone behind the disk. For $\chi = 20$, C_{Dv} gradually decreases to approximately zero as Re increases to 120; while C_{Dp} is still large although the wake disappears for the presented range of Re. At $\mathrm{Re} \leqslant 20$, C_{Dp} is almost the same for both χ, indicating that it is mainly the viscous force that contributes to the difference in the total drag between the two χ. In addition, the drag for $\chi = 20$ also satisfies Eq. (9) since the effects of vortex, viscous force, and momentum change are very small. The power law of $C_{Dp} \approxeq C_D \approxeq 8.5032\mathrm{Re}^{-0.561}$ is also shown in Fig. 9(d) for $\chi = 20$, which indicates that $U_a \propto \mathrm{Re}^{0.439}$ by substituting the power law into Eq. (9).

C. The bifurcation diagram

As presented in Sec. III B, the recirculating wake disappears when Da, χ, or Re is greater than a critical value. This indicates that the bifurcation diagram exists for any combinations of the parametric spaces of Re-Da, Da-χ, and Re-χ for the occurrence and disappearance of the recirculating wake. Figure 10(a) shows the Re-Da bifurcation diagram at various χ. For each bifurcation curve, the recirculating wake exists on the left side and does not exist on the other side. There exists a maximum Da_{max} that when $Da > Da_{max}$, no recirculating wake exists. The corresponding Re is denoted as Re_{max}. It is observed that the range of Da for the existence of recirculating wake is wider for smaller χ. Each bifurcation curve can be fitted into the equation [21]:

$$\mathrm{Da}(\mathrm{Re}) = \mathrm{Da}_{max}\exp[-c_1\ln^2(\mathrm{Re}/\mathrm{Re}_{max})]\exp[c_2(\mathrm{Re}/\mathrm{Re}_{max})^2 - 2c_2\ln(\mathrm{Re}/\mathrm{Re}_{max}) - c_2], \quad (10)$$

where the coefficients of Da_{max}, Re_{max} are presented in Table II for each χ. The Da_{max} for each curve decreases with increasing χ. The corresponding Re_{max} also decreases from 52 to 42 in the investigated range of χ. The fitting coefficients of $c_1 \approx 0.82$ and $c_2 \approx 0.098$ are found to be applicable for all χ.

It is also observed that the bifurcation curves in Fig. 10(a) are almost parallel to each other, suggesting that the difference in log(Da) between any two χ is nearly the same for all Re. By using linear interpolation, the Da at fixed Re is obtained for each χ. The variations of Da with χ at various Re are presented in Fig. 10(b). For all Re, Da decreases monotonically with χ, which tells that as χ increases, a smaller Da is required for the wake to be vanished. The bifurcation curve in the Da-χ plane, for each Re, can be expressed as $\log[\mathrm{Da}(\chi)] = -a\ln(\chi) + b$ by using the logarithmic fitting with the coefficient of determination $R^2 \sim 0.999$. The coefficients are $a \approx 0.431$ and $b \approx 2.1$ for all the presented Re. These bifurcation curves can be roughly collapsed onto the same curve, below

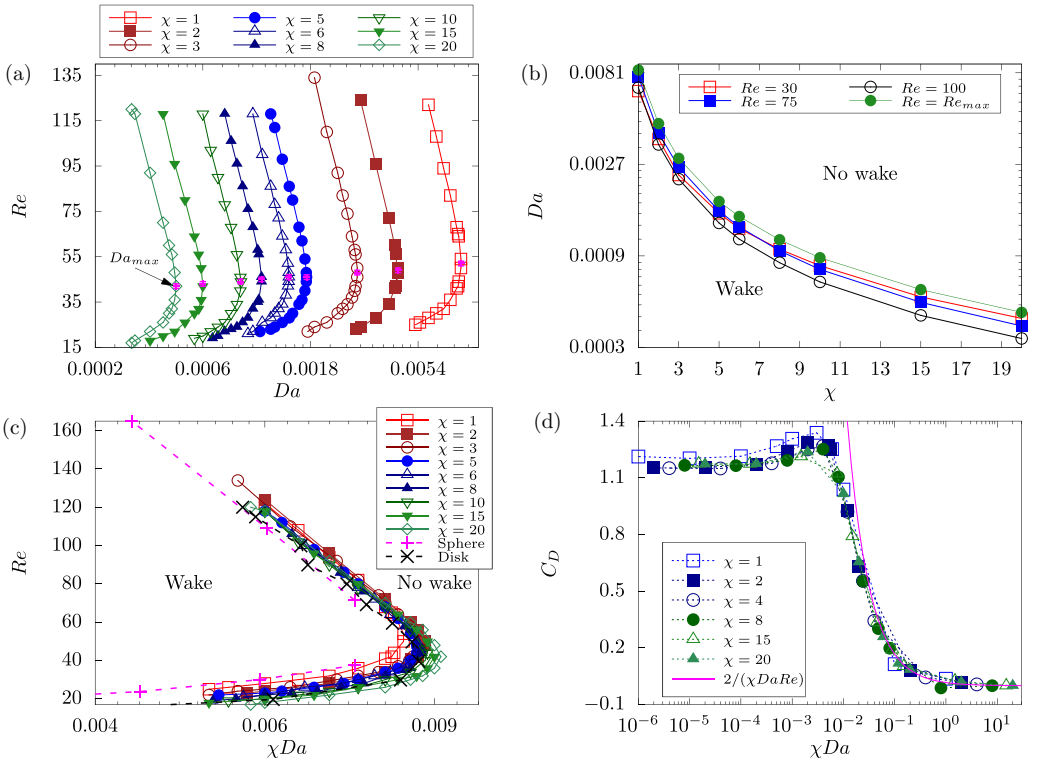

FIG. 10. (a) The Re-Da bifurcation diagram for the existence of recirculating wake at various χ; (b) the Da-χ bifurcation diagram at various Re; (c) the Re-χDa bifurcation diagrams of the present results (solid lines with various symbols) and the previous results (dashed lines with symbols + for sphere [14] and × for disk [21]) showing consistency in different axisymmetric bodies; (d) the C_D (calculated from CV) varying with χDa at different χ and fixed Re = 120.

which the recirculating wake exists and above which the recirculation zone disappears. Note that the $\mathrm{Da_{max}}$ can also be expressed as a function of χ for $\mathrm{Re} = \mathrm{Re_{max}}$, so that the effects of χ can be incorporated into Eq. (10). The logarithmic fitting curve also hinted that, for two arbitrary aspect ratios χ^* and χ^{**}, we have

$$\log[\mathrm{Da}(\chi^*)] - \log[\mathrm{Da}(\chi^{**})] = a[\ln(\chi^{**}) - \ln(\chi^*)], \tag{11}$$

which leads to

$$\ln[\mathrm{Da}(\chi^*)] - \ln[\mathrm{Da}(\chi^{**})] = a\ln 10[\ln(\chi^{**}) - \ln(\chi^*)] \approxeq \ln(\chi^{**}) - \ln(\chi^*), \tag{12}$$

where $a\ln 10 \approx 1$ for all Re. Therefore, we have

$$\chi^*\mathrm{Da}(\chi^*) \approxeq \chi^{**}\mathrm{Da}(\chi^{**}), \tag{13}$$

which suggests that χDa is approximately the same for the range of investigated χ at an arbitrarily fixed Re.

Equation (13) also indicates that the bifurcation curves varying with χDa can be roughly collapsed onto the same curve, as demonstrated in Fig. 10(c), especially for the intermediate χ with similar $\mathrm{Re_{max}}$. Since the bifurcation curve in the Da-χ plane is similar for all Re [Fig. 10(b)], Da on the bifurcation curve can be expressed as a function of only χ. Therefore, as observed in Fig. 10(c), Re can be expressed as a function of only χ or Da or vice versa. The effect of χ and Da on the flow is somewhat replaceable. The bifurcation curves for axisymmetric bodies in the

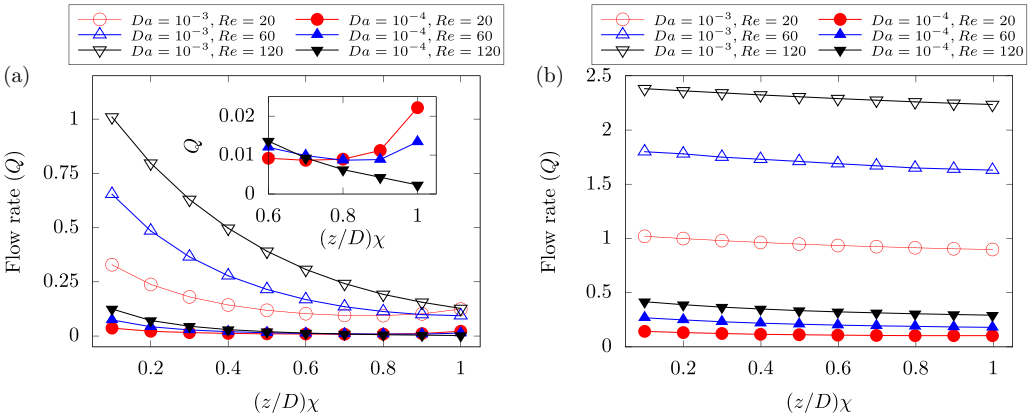

FIG. 11. Flow rate along with the vertical length of the porous disk for (a) $\chi = 2$ and (b) $\chi = 15$.

previous studies [14,21] are also presented in Fig. 10(c). The bifurcation curve for the porous disk with $\chi = 10$ [21] compares well with the present result, as expected. The bifurcation curve for the porous sphere [14] can also be collapsed onto that of the disk with $\chi = 1$ when Da is increased by a factor of 1.5 times. In this case the Da is modified by a shape factor which is calculated from the ratio of the volume of disk with $\chi = 1$ to the volume of the sphere with the same diameter.

The roughly collapsed bifurcation curves with respect to χDa were also reported for the nonaxisymmetric bodies of rectangular cylinders in Ref. [11], where the neutral stability curve was regarded as the bifurcation curve. However, the difference among the collapsed curves for the rectangular cylinders seems larger than that for the present axisymmetric bodies. Besides, one may be interested in the consistency between the axisymmetric and nonaxisymmetric bodies when χ is set to be the same, however, the bifurcation curves for the nonaxisymmetric bodies of square and circular cylinders [7,8] cannot be collapsed onto that of the disk (with $\chi = 1$) because of their intrinsic shape differences; also, the ranges of Re for the steady flow regime of the nonaxisymmetric bodies are much smaller than those of the axisymmetric bodies.

Since Da is closely related to the drag of the porous disk, the C_D for various χ is calculated at Re = 120, as presented in Fig. 10(d). Interestingly, C_D for all χ also approximately collapsed onto the same curve when varying with χDa. For very high permeability, this indicates that the shape factor of χ alters the drag exerted on the porous body. Equation (8) implies that, at the same Re, the larger χ disk requires smaller Da to achieve the same C_D as the smaller χ disk. If the modified χDa is employed, the drag exerted on the disk is approximately the same, and the bifurcation behaviors of the occurrence and disappearance of recirculating wake are similar among all χ. For relatively low permeability, this also suggests that the summation of the RHS terms of Eq. (7) is almost the same for fixed χDa.

D. The flow rate

The effects of χ on the volumetric flow rate (Q) through the porous circular disk are also investigated. Here, Q is calculated as the integration of u_z over the circular area for a particular z position, i.e.,

$$Q(z) = 2\pi \int_0^R u_z(r, z) r dr. \tag{14}$$

Figure 11(a) shows the variation of Q along with the nondimensional vertical length of the disk (z/D) at different Da and Re with fixed $\chi = 2$. For the presented Re, the Q at Da $= 10^{-4}$ is close to zero due to the large obstructing effects in the porous medium. The Q at Da $= 10^{-3}$ is noticeably

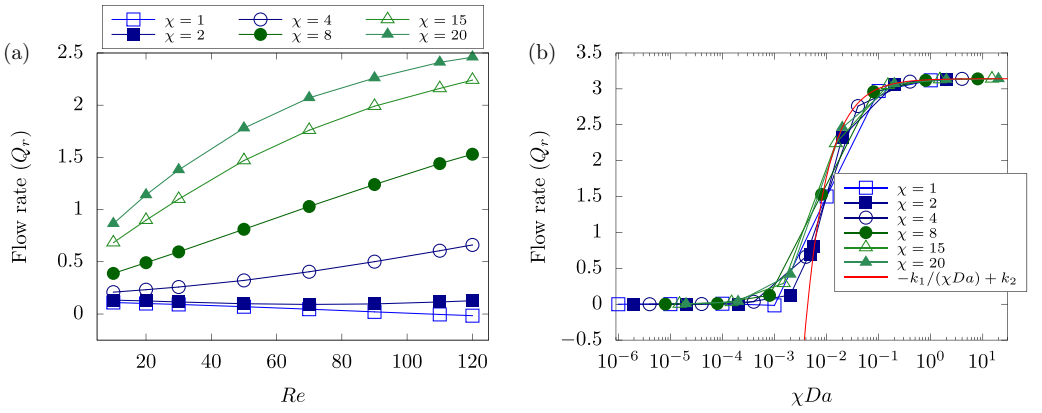

FIG. 12. Flow rate at the rear surface of the porous disk (Q_r) varying with (a) Re for Da $= 10^{-3}$ and (b) Da for Re $= 120$.

larger than those at Da $= 10^{-4}$ for the range of z/D, as expected. For both Da, Q is observed to first decreases and then increases with z/D when Re is relatively small, as clearly seen in the zoom-in plot. While for larger Re, Q decreases monotonically with z/D. This is because, for a small Re, the flow velocity in most part of the passageway is low except that near the outer boundaries of the porous disk where an increase transition to the free-stream velocity is required. As the distance z/D increases, the inertial effects from the outer flow exceed the obstructing effect of the porous medium, giving rise to a larger Q. However, for a large Re, the flow velocity in the middle part of the passageway is fairly large, which decreases gradually along the radial direction due to the porous disk wall. The increment of velocity near the outer boundary also exists due to the free-stream flow. Along with z/D, the obstructing effects from the porous disk wall outstrips the inertial effects from the outer flow so that Q continue decreasing.

Figure 11(b) shows the variation of Q along with z/D at fixed $\chi = 15$. Different from the thicker disk, the Q decreases slightly and almost linearly with the distance z/D for all cases, demonstrating that the obstructing effects of the thinner disk are much smaller than those of the thicker disk under the same Da and Re. The trivial difference of Q between the front and rear surfaces of the porous disk also suggests a small pressure drag. The variation trends of Q with Re and Da are also similar to those in Fig. 11(a). Since the distance z/D of a thin disk is too short for flow development, the variation trend of Q along z/D here is simpler compared to those in Fig. 11(a). Also, the large Q at the rear surface of the disk implies a large amount of base bleed, which may prevent the recirculation formation behind the disk.

The flow rate through the rear surface of the porous disk (Q_r) is also calculated for various Re and Da since the base bleed from a porous bluff body was found to have large effect on the wake structure behind the body [7,8]. Figure 12(a) shows the variation of Q_r with Re at different χ. For $\chi \leqslant 2$, Q_r is close to zero for the presented range of Re, which is owing to the reverse flow penetrating the rear surface. As Re increases, the recirculating wake becomes larger, bringing more reverse flow into the thick porous disk. The thicker the disk becomes, the smaller the velocity will be at the rear surface so that it is more difficult to resist the reverse flow. This is revealed in the observed trends that Q_r decreases monotonically with Re for $\chi = 1$; while Q_r first decreases and then increases with Re for $\chi = 2$. For larger χ of 4 and 8, Q_r increases almost linearly with Re since the thin disk does not have much impedance on the flow. For $\chi = 8$, we have $Q_r = 0.021\mathrm{Re} + 0.286$. For larger $\chi \geqslant 15$, the linear relationship between Q_r and Re is not satisfied and Q_r increases slowly for larger Re, which is due to the upper bound of the flow rate, i.e., the free stream velocity flow rate.

Note that the linear relationship may occur at different χ for different Da. For instance, we have $Q_r = 0.0055\mathrm{Re} + 0.0854$ for $\chi = 20$ and Da $= 10^{-4}$. For particular χ and Da, usually at

relatively large χ and small Da, the u_z is nearly constant within the porous disk except at the boundary between the porous disk and the clear fluid. Therefore, it is reasonable to assume that $Q_r = \pi r^2 u_z(\mathrm{Re}) + B(\mathrm{Re})$, where $B(\mathrm{Re})$ is the part affected by the flow at the fluid-porous interface. Considering the Darcy law within the porous medium, i.e., $u_z = K\nabla p/\mu$ (∇p is pressure gradient), the formula can be expressed as $Q_r = A\mathrm{Re} + B(\mathrm{Re})$ with $A = (\pi r^2 \nabla p \mathrm{Da} D)/(\rho U_\infty)$. The coefficient A can be a constant if ∇p is not affected by Re, which seems applicable from Fig. 11(b). Since u_z is dominant in the porous medium, the effects of Re on the part of flow near the boundary is assumed to be negligible so that $B(\mathrm{Re})$ is a constant. Therefore, the linear relationship with Re is recovered. However, for a small χ, the u_z varies greatly with r due to the boundary effects, thus the assumption of uniform u_z within the porous medium is not valid. For a large Da, the boundary flow is largely affected by Re, so that $B(\mathrm{Re})$ is not a constant. In these cases, the linear relationship of Q_r with Re does not exist.

Figure 12(b) presents the variation of Q_r with $\chi\mathrm{Da}$ at fixed $\mathrm{Re} = 120$. As χ increases, the flow rate becomes larger at a smaller Da. Interestingly, the Q_r curves of all χ can also be roughly collapsed onto the same curve, similar to the bifurcation curves. The Q_r first increases slowly for relatively small Da, and then increases greatly for an intermediate range of Da, and after that increases slowly again for a large Da. For the high permeable cases, the curves can be fitted into $Q_r = -k_1/(\chi\mathrm{Da}) + k_2$, where the coefficients $k_1 = 0.0136$ and $k_2 = 3.1418$. The expression is very similar to that of C_D at high permeability limit [Eq. (8)]. Indeed, the Q_r is closely related to C_D since it greatly affects the wake structure. Therefore, the collapsed curves of Q_r are consistent with the collapsed curves of C_D [Fig. 10(d)].

E. Vorticity generation and attenuation

The vorticity accumulation was demonstrated to be closely linked to the wake structure behind the porous body, as discussed in Refs. [14,46]. Vorticity is mainly generated from the no-slip condition and the surface curvature. Also, the vorticity decay, along with vorticity accumulation contribute to the formation of the recirculating wake, as analyzed in Ref. [46] for a group of circular cylinders. In this section, the vorticity is examined for the 2D axisymmetric flow in an attempt to interpret the wake signature at different Re, Da, and χ. Figure 13 shows a slice of the dimensionless vorticity field $\Omega(r, z)D/U_\infty$ in the negative azimuthal direction, where $\Omega(r, z) = \partial u_z/\partial r - \partial u_r/\partial z$, at representative χ under different Re and Da. The same range of vorticity [0.2, 4.68] and the same area of interest $(r/D) \times (z/D) \in [0, 1.25] \times [-0.25, 1]$ are used for all cases.

Figures 13(a)–13(c) show the vorticity distribution χ of 2, 8, 20, respectively, at fixed $\mathrm{Da} = 10^{-3}$ and $\mathrm{Re} = 30$. For all cases, the large vorticity is accumulated about the top left corner of the porous disk. Also, the position of the largest vorticity moves gradually towards the downstream side as χ increases. The vorticity layers in front of and on the lateral side of the disk also become thinner with an increment in χ. The overall vorticity in the region of interest is relatively small for larger χ. All these indicate that a larger χ at the specific Da and Re is much easier for flow to pass through. For a larger $\mathrm{Re} = 120$, the tendency with increasing χ is even more obvious, as shown in Figs. 13(d)–13(f). For the larger Re, the vorticity layers become thinner for all cases. The vorticity is easily advected downstream and the vorticity peak moves further downstream, especially for $\chi = 8$ and 20, where the vorticity peak occurs at the right corner of the porous disk. For smaller $\mathrm{Da} = 10^{-4}$ at $\mathrm{Re} = 120$ in Figs. 13(g)–13(i), the vorticity layers and vorticity values are similar for all disks. The increasing χ does not have weakening effects. It is also observed that the negative vorticity is accumulated on the rear side of the disk and the peak of the negative vorticity moves to the right corner of the disk as χ increases. The largest vorticity all reside near the left corner of the disk. Compared with the larger Da cases, smaller Da obviously produces more vorticity.

The vorticity peak, defined as $\Omega_p = \max_{0<r<20D,\,-19.5D<z<20.5D}(\Omega D/U_\infty)$, is also obtained at various Re and Da for representative χ. Figure 14(a) shows the variations of Ω_p with Re at two fixed Da. For relatively small $\mathrm{Da} = 10^{-4}$, Ω_p is roughly the same for all the presented χ, which demonstrates an monotonically increasing trend with Re since the stronger velocity gradient

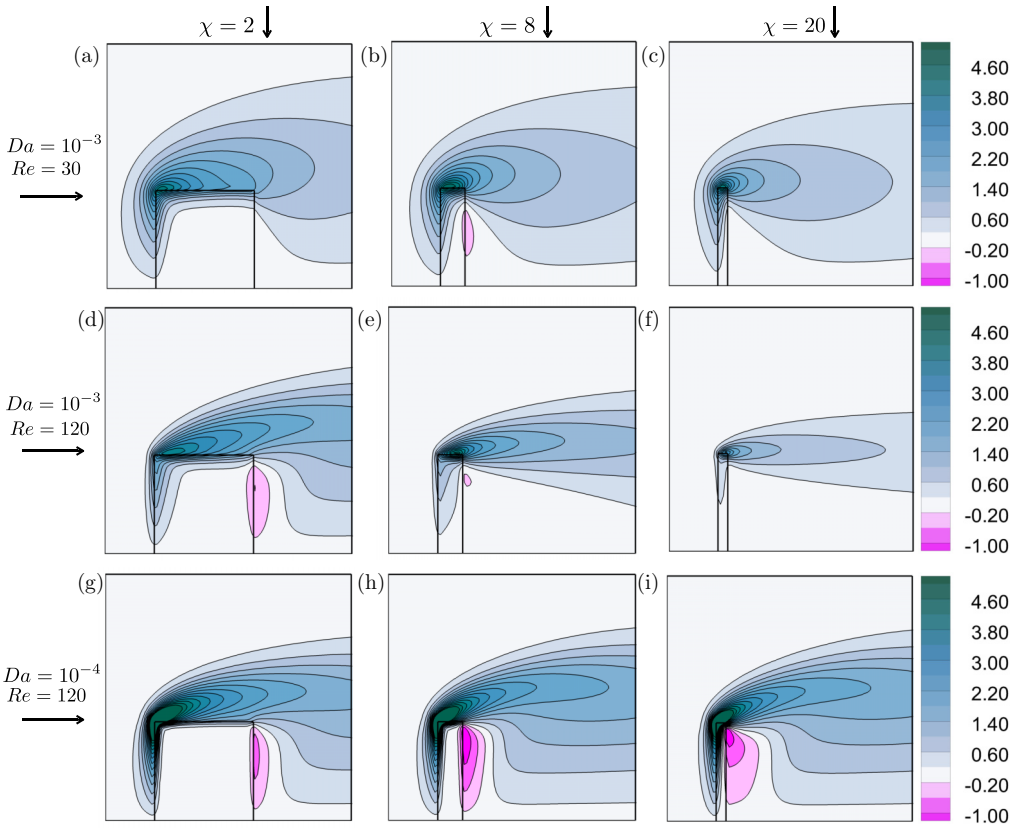

FIG. 13. The dimensionless vorticity field $|\Omega(r, z)|D/U_\infty$ for (a, d, g) $\chi = 2$, (b, e, h) $\chi = 8$, (c, f, i) $\chi = 20$ at different Da and Re as indicated on the left.

produces larger vorticity. A crossover point is also observed at Re ≈ 70 for various χ with fixed Da $= 10^{-4}$. For Re $\lessapprox 70$, Ω_p increases with increasing χ, while for Re $\gtrapprox 70$, Ω_p decreases with increasing χ. The reason for this may be that, for smaller Re, the curvature of bluff body produces more vorticity than the velocity gradient at the surface, while for larger Re, the velocity gradient becomes dominant over the curvature effects in vorticity generation. For relatively large Da $= 10^{-3}$,

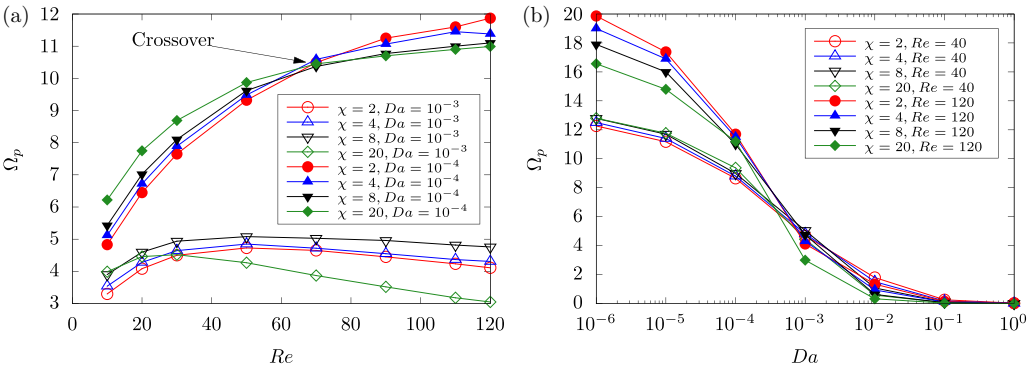

FIG. 14. Variations of Ω_p with (a) Re and (b) Da at different χ as indicated.

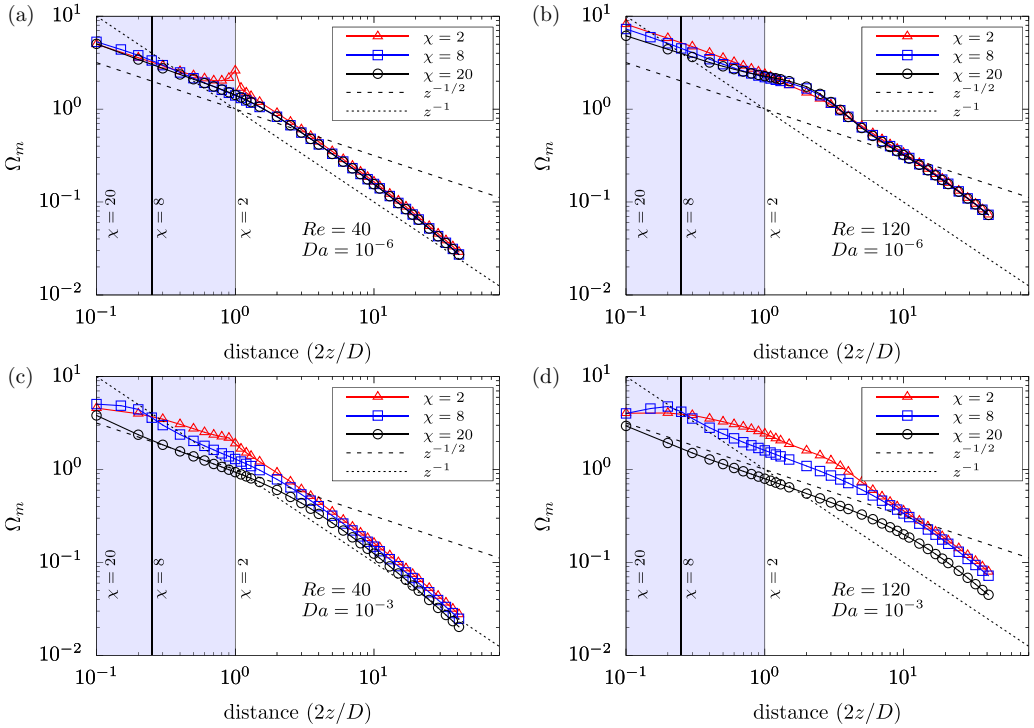

FIG. 15. Variation of Ω_m with downstream distance at different χ, Re and Da as indicated.

the nonmonotonous trend of Ω_p with Re is observed for all χ. The increasing Re indicates that more vorticity is generated in the boundary layer developed on the front surface of the disk; however as Re further increases, the vorticity is advected through the porous disk with weakened boundary layer, resulting in smaller Ω_p. Overall, the Ω_p is much smaller than that at lower permeability. The Ω_p is also observed to increase with increasing χ for $\chi = 2, 4, 8$, while the Ω_p for $\chi = 20$ is much smaller.

Figure 14(b) shows the variation of Ω_p with Da at two fixed Re. For relatively small Re $= 40$, the Ω_p for all χ decrease with increasing Da, which is expected since larger permeability allows more flow through the disk and therefore more vorticity is advected downstream. Also, the Ω_p for all χ are almost the same with small differences, which indicates that the curvature of large χ and the longer side surface of smaller χ have similar effects on the vorticity accumulation. For relatively large Re $= 120$, the Ω_p also decreases with increasing permeability with a larger decreasing rate than that at smaller Re since the combination effects of large Da and Re gives rise to larger vorticity advection. For smaller Da, the Ω_p is evidently larger at smaller χ since more vorticity is generated at the surface. As Da becomes larger, the difference among χ is more trivial.

The vorticity decay with the downstream distance is also investigated to further understand the wake behaviors. The variations of the maximum vorticity (Ω_m), defined as $\Omega_m(z) = \max_{0<r<20D}(\Omega D/U_\infty)$, with downstream distance $(2z/D)$ at representative χ, Re, and Da are presented in Fig. 15. The two main processes that lead to decreased Ω_m are diffusion and vorticity annihilation, which correspond to decay rates of $z^{-1/2}$ and z^{-1}, respectively [39,46]. Therefore, the decay laws are also presented in each part of Fig. 15 for the ease of comparison. Besides, the vertical lines at $2z/D = 0.1, 0.25, 1.0$ are drawn to represent the rear surfaces of the porous disk with $\chi = 20, 8, 2$, respectively, so that the shaded area on the left side of the vertical line represents the porous region for a specific χ.

For relatively small $\mathrm{Da} = 10^{-6}$ and $\mathrm{Re} = 40$ [Fig. 15(a)], the vorticity profiles for all the presented χ are almost collapsed onto the same line, except for an obvious jump occurring at the rear surface for $\chi = 2$. The sudden increase in Ω_m is mainly due to the vorticity accumulation along the side surface, which is longer for smaller χ, as well as the sharp corner of the porous disk. For $0.1 \leqslant 2z/D \lesssim 2$, the decay rates of all χ follow the $z^{-1/2}$ law although the range of distance indicates different media for various χ, i.e., complete wake flow for $\chi = 20$, partial wake flow for $\chi = 8$, and near-complete porous medium for $\chi = 2$. With the presence of porous media, this slower decay is mainly due to the skin friction on the porous surface; otherwise, the slower decay is mainly supported by the entrained fluid flow from the outside, which forms the recirculation zone. For $2z/D \gtrsim 2$, where the vorticity is $\lesssim 20\%$ of the original value (at $2z/D = 0.1$), the decay rates gradually transition to be equal to or even higher than z^{-1}. This suggests that the diffusive recirculating wake right behind the rear surface of the porous disk is longer for larger χ since the axial position of the rear surface is smaller for larger χ, while the axial position of the decay-rate-transition point is almost the same for all the presented χ.

As Re increases to 120 while keeping the Da fixed at 10^{-6} [Fig. 15(b)], the Ω_m within the downstream distance is overall larger compared with the Ω_m presented in Fig. 15(a). The decay rates for all χ are almost collapsed onto the same line, especially for the clear fluid flow region. The sudden increase at the rear surface for $\chi = 2$ is not presented since more vorticity is advected to the downstream with the larger inertial force. With the same decay rate of $z^{-1/2}$ for the first 80% decrement of vorticity, the decaying distance here is larger since the Ω_m at $2z/D = 0.1$ is comparatively larger than the smaller Re cases in Fig 15(a). The larger decaying distance also indicates longer recirculating wake due to diffusion. The faster decay follows the z^{-1} law exactly due to the intermingle of positive and negative vorticity. Also, the wake length for thinner disk can be larger due to the formation of recirculation zone right behind the rear surface of the disk, as stated above.

For relatively large permeability ($\mathrm{Da} = 10^{-3}$) at $\mathrm{Re} = 40$, the difference in Ω_m among all the presented χ becomes larger, especially within the downstream distance of slower decay, as seen in Fig. 15(c). Under this circumstance, more fluid flows through the porous disk with larger velocity, interacting with the viscous flow near the porous-walls and contributing to more vorticity generation. Therefore, the decay rate with the presence of porous media for $\chi = 2, 8$ is even smaller than the decay law of $z^{-1/2}$. For $\chi = 2$, a small bump is also shown at the rear surface of the porous disk, though much flatter than that in Fig. 15(a). The vorticity also decays to approximately 20% of its original value. The decaying distance also becomes larger since the porous medium raises the vorticity to some extent for $\chi = 2, 8$. For $\chi = 8$, the vorticity first decreases very slowly in the porous region, and then decays faster after the rear surface. A larger amount of fluid flow through the disk so that a shear layer is formed by the base bleed flow and the flow outside of the disk, resulting a smaller recirculating wake further downstream. For $\chi = 20$, the vorticity first decreases following the $z^{-1/2}$ law, and then decreases with the z^{-1} law. There is sufficiently large amount of fluid flowing out of the rear surface, supporting the diffusion decay, therefore no fluid is entrained to the near wake.

Figure 15(d) shows the vorticity decay at relatively large $\mathrm{Re} = 120$ and the same $\mathrm{Da} = 10^{-3}$ with Fig. 15(c). The effects of inertial force on the flow within the porous region is more significant. It is observed that although the vorticity at $2z/D = 0.1$ is similar for all χ, it further increases for $\chi = 2, 8$ within its corresponding porous regions, while decreases with the $z^{-1/2}$ law for $\chi = 20$. The increasing vorticity also somewhat elongates the decaying distance. For $\chi = 2$, since the base bleed flow velocity is small, the recirculating wake forms due to the fluid entrainment. For larger $\chi = 8, 20$, the base bleed is even larger at $\mathrm{Re} = 120$, which is sufficient to remain the diffusion decay rate, and therefore the vortex is not formed behind the disk.

IV. SUMMARY AND CONCLUSIONS

The problem of steady axisymmetric flow through and around a porous disk is solved numerically with a porous-fluid coupling method. The present results are verified and validated for both

impermeable and permeable cases. The interplay of three important nondimensional parameters: χ, Re, Da, are investigated with a focus on the wake structure and the drag exerted on the porous disk. In particular, the influence of χ on the flow behavior is studied in terms of the streamline patterns, the geometrical parameters of recirculating wake, drag components, and the bifurcation diagram in the investigated parametric space.

For low permeable cases, the recirculating wake behind a thinner disk (larger χ) is longer than that behind a thicker disk (smaller χ); while the opposite trend is observed for high permeable cases. The variations of the geometrical parameters with Da, χ, Re all imply that the recirculating wake would disappear when the nondimensional parameters are greater than the corresponding critical values. The drag is calculated from both the SI and the CV methods. The SI method is found to underestimate the total drag due to neglecting the momentum change. The effects of the Darcy flow through the porous disk, the vortex behind the disk, the shear stress on the porous boundaries, and the momentum change are discussed with regards to their contributions to the total drag. The bifurcation diagrams in the Re-Da parametric space for all the investigated χ can be collapsed approximately into the same curve in the Re-χDa space. Also, the bifurcation diagrams in the Da-χ space for all Re can be collapsed roughly into the same power law curve. This indicates that χ and Da are somewhat replaceable, which modifies the drag exerted on the porous disk and affects the existence of recirculating wake. Also, C_D is observed to be approximately the same for a particular fixed χDa.

The flow rate and vorticity are also investigated to further understand the wake behaviors. It is demonstrated that the base bleed (flow rate at the rear surface of the disk), which increases with all the controlling parameters of Re, χ, Da, directly affects the recirculating wake formation. The rear flow rates are almost the same for a wide range of χ when varying with χDa since the Q_r is closely related with the drag exerted by the fluid. Furthermore, it is found that the vorticity accumulation is mainly affected by Da and Re, which does not differ much among all the χ. Also, for all presented cases, the vorticity decay follows the $z^{-1/2}$ law until the vorticity is decreased to $\sim$20% of its original value at $2z/D = 0.1$. The slower decay rate requires sufficient entrainment of fluids behind the porous disk, which is satisfied by forming a recirculating wake for low permeable cases, and by the large amount of base bleed for high permeable cases.

Finally, it is noted that the results and regular patterns for the porous disk in the present study may also be applicable for the oblate spheroid and even the nonaxisymmetric bodies, as partially demonstrated previously for flow through and around a porous rectangular cylinder in Ref. [11]. It should also be mentioned that the steady axisymmetric assumption, made under the current ranges of controlling parameters, is based on flow around an impermeable disk. The transition parameters to steady nonaxisymmetric and unsteady flow regimes are expected to be different for permeable cases, which will be studied with 3D simulations in the future.

ACKNOWLEDGMENTS

The authors appreciate the financial support from NSFC (Grants No. 11672124 and No. 12002148), the Shenzhen Peacock Plan (Grant No. KQTD2016022620054656), Guangdong Provincial Key Laboratory of Turbulence Research and Applications (Grant No. 2019B21203001), and Shenzhen Key Laboratory of Complex Aerospace Flows (Grant No. ZDSYS201802081843517). This work is also supported by the Center for Computational Science and Engineering of Southern University of Science and Technology. The authors thank Dr. Y. Zeng from NMC, ASTAR, for her valuable discussion.

[1] C. Ellington, Wing mechanics and take-off preparation of thrips (thysanoptera), J. Exp. Biol. **85**, 129 (1980).

[2] C. Cummins, M. Seale, A. Macente, D. Certini, E. Mastropaolo, I. M. Viola, and N. Nakayama, A separated vortex ring underlies the flight of the dandelion, Nature (London) **562**, 414 (2018).
[3] J. H. Masliyah and M. Polikar, Terminal velocity of porous spheres, Can. J. Chem. Eng. **58**, 299 (1980).
[4] P. Yu, T. S. Lee, Y. Zeng, and H. T. Low, Fluid dynamics and oxygen transport in a micro-bioreactor with a tissue engineering scaffold, Int. J. Heat Mass Transf. **52**, 316 (2009).
[5] P. D. Noymer, L. R. Glicksman, and A. Devendran, Drag on a permeable cylinder in steady flow at moderate Reynolds numbers, Chem. Eng. Sci. **53**, 2859 (1998).
[6] S. Bhattacharyya, S. Dhinakaran, and A. Khalili, Fluid motion around and through a porous cylinder, Chem. Eng. Sci. **61**, 4451 (2006).
[7] P. Yu, Y. Zeng, T. S. Lee, X. B. Chen, and H. T. Low, Steady flow around and through a permeable circular cylinder, Comput. Fluids **42**, 1 (2011).
[8] P. Yu, Y. Zeng, T. Lee, H. Bai, and H. Low, Wake structure for flow past and through a porous square cylinder, Int. J. Heat Fluid Flow **31**, 141 (2010).
[9] M. S. Valipour, S. Rashidi, M. Bovand, and R. Masoodi, Numerical modeling of flow around and through a porous cylinder with diamond cross section, Eur. J. Mech. B/Fluids **46**, 74 (2014).
[10] T. Tang, P. Yu, S. Yu, X. Shan, and H. Chen, Connection between pore-scale and macroscopic flow characteristics of recirculating wake behind a porous cylinder, Phys. Fluids **32**, 083606 (2020).
[11] P. G. Ledda, L. Siconolfi, F. Viola, F. Gallaire, and S. Camarri, Suppression of von Kármán vortex streets past porous rectangular cylinders, Phys. Rev. Fluids **3**, 103901 (2018).
[12] G. Neale, N. Epstein, and W. Nader, Creeping flow relative to permeable spheres, Chem. Eng. Sci. **28**, 1865 (1973).
[13] K. Nandakumar and J. H. Masliyah, Laminar flow past a permeable sphere, Can. J. Chem. Eng. **60**, 202 (1982).
[14] P. Yu, Y. Zeng, T. S. Lee, X. B. Chen, and H. T. Low, Numerical simulation on steady flow around and through a porous sphere, Int. J. Heat Fluid Flow **36**, 142 (2012).
[15] T. Zlatanovski, Axisymmetric creeping flow past a porous prolate spheroidal particle using the Brinkman model, Q. J. Mech. Appl. Math. **52**, 111 (1999).
[16] P. Vainshtein, M. Shapiro, and C. Gutfinger, Creeping flow past and within a permeable spheroid, Int. J. Multiphase Flow **28**, 1945 (2002).
[17] P. K. Yadav and S. Deo, Stokes flow past a porous spheroid embedded in another porous medium, Meccanica **47**, 1499 (2012).
[18] E. Barta and D. Weihs, Creeping flow around a finite row of slender bodies in close proximity, J. Fluid Mech. **551**, 1 (2006).
[19] T. Uchida, Y. Taniyama, Y. Fukatani, M. Nakano, Z. Bai, T. Yoshida, and M. Inui, A new wind turbine CFD modeling method based on a porous disk approach for practical wind farm design, Energies **13**, 3197 (2020).
[20] M. Liu, C. Xie, M. Yao, and J. Yang, Study on the near wake of a honeycomb disk, Exp. Therm. Fluid Sci. **81**, 33 (2017).
[21] C. Cummins, I. M. Viola, E. Mastropaolo, and N. Nakayama, The effect of permeability on the flow past permeable disks at low Reynolds numbers, Phys. Fluids **29**, 097103 (2017).
[22] P. G. Ledda, L. Siconolfi, F. Viola, S. Camarri, and F. Gallaire, Flow dynamics of a dandelion pappus: A linear stability approach, Phys. Rev. Fluids **4**, 071901(R) (2019).
[23] D. Fabre, F. Auguste, and J. Magnaudet, Bifurcations and symmetry breaking in the wake of axisymmetric bodies, Phys. Fluids **20**, 051702 (2008).
[24] R. Natarajan and A. Acrivos, The instability of the steady flow past spheres and disks, J. Fluid Mech. **254**, 323 (1993).
[25] F. W. Roos and W. W. Willmarth, Some experimental results on sphere and disk drag, AIAA J. **9**, 285 (1971).
[26] P. Meliga, J.-M. Chomaz, and D. Sipp, Global mode interaction and pattern selection in the wake of a disk: A weakly nonlinear expansion, J. Fluid Mech. **633**, 159 (2009).
[27] S. Gao, L. Tao, X. Tian, and J. Yang, Flow around an inclined circular disk, J. Fluid Mech. **851**, 687 (2018).

[28] A. Shenoy and C. Kleinstreuer, Flow over a thin circular disk at low to moderate Reynolds numbers, J. Fluid Mech. **605**, 253 (2008).
[29] F. Auguste, D. Fabre, and J. Magnaudet, Bifurcations in the wake of a thick circular disk, Theor. Comput. Fluid Dyn. **24**, 305 (2010).
[30] M. Chrust, G. Bouchet, and J. Dusek, Parametric study of the transition in the wake of oblate spheroids and flat cylinders, J. Fluid Mech. **665**, 199 (2010).
[31] P. C. Fernandes, F. Risso, P. Ern, and J. Magnaudet, Oscillatory motion and wake instability of freely rising axisymmetric bodies, J. Fluid Mech. **573**, 479 (2007).
[32] W. W. Willmarth, N. E. Hawk, and R. L. Harvey, Steady and unsteady motions and wakes of freely falling disks, Phys. Fluids **7**, 197 (1964).
[33] K. Vafai and C. L. Tien, Boundary and inertia effects on flow and heat transfer in porous media, Int. J. Heat Mass Transf. **24**, 195 (1981).
[34] S. Whitaker, Flow in porous media I: A theoretical derivation of Darcy's law, Transp. Porous Media **1**, 3 (1986).
[35] S. Whitaker, The Forchheimer equation: A theoretical development, Transp. Porous Media **25**, 27 (1996).
[36] J. A. Ochoa-Tapia and S. Whitaker, Momentum transfer at the boundary between a porous medium and a homogeneous fluidi. theoretical development, Int. J. Heat Mass Transf. **38**, 2635 (1995).
[37] P. Nithiarasu, K. N. Seetharamu, and T. Sundararajan, Natural convective heat transfer in a fluid saturated variable porosity medium, Int. J. Heat Mass Transf. **40**, 3955 (1997).
[38] J. Alberto, Momentum jump condition at the boundary between a porous medium and a homogeneous fluid: Inertial effects, J. Porous Media **1**, 3 (1998).
[39] A. Nicolle and I. Eames, Numerical study of flow through and around a circular array of cylinders, J. Fluid Mech. **679**, 1 (2011).
[40] P. K. Kundu and I. M. Cohen, *Fluid Mechanics*, 4th ed. (Elsevier, Burlington, MA, 2008).
[41] J. P. Van Doormaal and G. D. Raithby, Enhancements of the simple method for predicting incompressible fluid flows, Numer. Heat Transfer **7**, 147 (1984).
[42] C. Rhie and W. L. Chow, Numerical study of the turbulent flow past an airfoil with trailing edge separation, AIAA J. **21**, 1525 (1983).
[43] P. Yu, T. S. Lee, Y. Zeng, and H. T. Low, A numerical method for flows in porous and homogenous fluid domains coupled at the interface by stress jump, Int. J. Numer. Methods Fluids **53**, 1755 (2007).
[44] A. Sohankar, C. Norberg, and L. Davidson, Low-Reynolds-number flow around a square cylinder at incidence: Study of blockage, onset of vortex shedding and outlet boundary condition, Int. J. Numer. Methods Fluids **26**, 39 (1998).
[45] C. Cummins, I. M. Viola, E. Mastropaolo, and N. Nakayama, Erratum: The effect of permeability on the flow past permeable disks at low Reynolds numbers, Phys. Fluids **32**, 119901 (2020).
[46] T. Tang, P. Yu, X. Shan, and H. Chen, The formation mechanism of recirculating wake for steady flow through and around arrays of cylinders, Phys. Fluids **31**, 043607 (2019).
[47] T. Tang, P. Yu, X. Shan, H. Chen, and J. Su, Investigation of drag properties for flow through and around square arrays of cylinders at low Reynolds numbers, Chem. Eng. Sci. **199**, 285 (2019).
[48] Z. G. Feng and E. E. Michaelides, Motion of a permeable sphere at finite but small Reynolds numbers, Phys. Fluids **10**, 1375 (1998).